GLIA

WILEY

RESEARCH ARTICLE

HIF prolyl hydroxylase 2/3 deletion disrupts astrocytic integrity and exacerbates neuroinflammation

Kamil Sebastian Rosiewicz[1] | Bakhrom Muinjonov[1] | Séverine Kunz[2] |
Helena Radbruch[3] | Jessy Chen[1,4] | René Jüttner[5] | Janis Kerkering[1] |
Julia Ucar[1] | Tadhg Crowley[1] | Ben Wielockx[6] | Friedemann Paul[1] |
Marlen Alisch[1] | Volker Siffrin[1,4]

[1]Experimental and Clinical Research Center
(ECRC), Charité—Universitätsmedizin Berlin
und Max Delbrück Center or Molecular
Medicine in the Helmholtz Association,
Berlin, Germany

[2]Technology Platform for Electron
Microscopy, Max Delbrück Centre for
Molecular Medicine in the Helmholtz
Association (MDC), Berlin, Germany

[3]Department of Neuropathology, Charité—
Universitätsmedizin Berlin., Berlin, Germany

[4]Department of Neurology, Charité
Universitätsmedizin Berlin., Berlin, Germany

[5]Neuromuscular and Cardiovascular Cell
Biology Group, Max-Delbrück-Center for
Molecular Medicine, Berlin, Germany

[6]Institute for Clinical Chemistry and
Laboratory Medicine, Technische Universität
Dresden., Dresden, Germany

Correspondence
Volker Siffrin, Experimental and Clinical
Research Center (ECRC), Charité—
Universitätsmedizin Berlin und Max-Delbrück-
Centrum für Molekulare Medizin, Berlin,
Lindenberger Weg 80, 13125 Berlin, Germany.
Email: volker.siffrin@charite.de

Abstract

Astrocytes constitute the parenchymal border of the blood–brain barrier (BBB), modulate the exchange of soluble and cellular elements, and are essential for neuronal metabolic support. Thus, astrocytes critically influence neuronal network integrity. In hypoxia, astrocytes upregulate a transcriptional program that has been shown to boost neuroprotection in several models of neurological diseases. We investigated transgenic mice with astrocyte-specific activation of the hypoxia-response program by deleting the oxygen sensors, HIF prolyl-hydroxylase domains 2 and 3 (Phd2/3). We induced astrocytic Phd2/3 deletion after onset of clinical signs in experimental autoimmune encephalomyelitis (EAE) that led to an exacerbation of the disease mediated by massive immune cell infiltration. We found that Phd2/3-ko astrocytes, though expressing a neuroprotective signature, exhibited a gradual loss of gap-junctional Connexin-43 (Cx43), which was induced by vascular endothelial growth factor-alpha (Vegf-a) expression. These results provide mechanistic insights into astrocyte biology, their critical role in hypoxic states, and in chronic inflammatory CNS diseases.

KEYWORDS
astrocyte, experimental autoimmune encephalomyelitis, hypoxia, multiple sclerosis, neuroprotection, PHD2/PHD3

1 | INTRODUCTION

Multiple sclerosis (MS) is the most common chronic inflammatory CNS disease worldwide. The pathology encompasses inflammatory focal lesions with immune-cell invasion, demyelination, and relative sparing of the neuronal compartment. However, as the disease progresses more and more axons and their processes are lost, which is the correlate of irreversible clinical deficits in these patients (Siffrin, Vogt, et al., 2010). The mechanistic role of metabolic factors, such as the availability of oxygen and glucose, has been a matter of controversial debate. Clearly, these factors could contribute, not only to the primary ischemic diseases namely stroke, but also to primary

neurodegenerative and neuroinflammatory diseases (Correia & Moreira, 2010; Trapp & Stys, 2009). The cellular response following hypoxia is an evolutionarily conserved process (Pelster & Egg, 2018), which has both intrinsic roles (cell survival by adaptation of metabolism) and extrinsic roles (improvement in oxygen provision). The CNS is a highly oxygenation-sensitive tissue with a very short hypoxia time until irreversible deficits develop. Therefore, metabolically active invading immune cells are a metabolic challenge for the CNS (Davies et al., 2013). Furthermore, the partial or complete demyelination of axons in MS infers a higher energy demand for upholding axon potential transmission (Trapp & Stys, 2009). The term "virtual hypoxia" has been coined as potential cause for axon degeneration in chronic inflammatory demyelinating CNS diseases.

The translational response of cells to low oxygen pressure is dependent on the hypoxia inducible factors (Hifs); the heterodimers combine either Hif1α or Hif2α with Hifβ. While Hifβ is constitutively present in the nucleus, Hifα activity is tightly regulated on the protein level by a rapid inactivation and degradation by the proteasome. Hifs bind to hypoxia response elements (HRE) that start the transcription of a characteristic cascade of hypoxia relevant genes, which serve to acutely handle hypoxia, such as switching from oxidative phosphorylation to glycolysis (e.g., via Ldh up-regulation). However, they also improve oxygen provision, including vascularization (e.g., via Vegf-a up-regulation) and erythropoiesis (e.g., via Erythropoeitin (Epo)). Hif1α is expressed by most cells in the organism whereas Hif2α expression is more restricted to specific cell populations, for example, kidney cells, myelopoietic cells, Müller glia, astrocytes, microglia, neuronal and endothelial cells (Jonz et al., 2016; Korovina et al., 2019; Toriuchi et al., 2020; Watts et al., 2020). The prolyl 4-hydroxylase domain (Phd) proteins are the pacemakers of Hif1α degradation, as they add the hydroxyl groups to Hif1α that enable binding of the Von Hippel Lindau (VHL) protein that initiates the final degradation process (Berra et al., 2003). Phds are highly sensitive to oxygen concentration; their activity strongly decreases in hypoxia. Phd2 is the main enzyme inducing Hif1α and Hif2α degradation under normoxic conditions. Phd3, as Hif1α induced gene product, is more relevant for regulation of Hif2α under hypoxia (Wielockx et al., 2019). Depletion of Phd2 and Phd3 has therefore been shown to strongly activate Hif1α and Hif2α driven gene expression (Urrutia et al., 2016). Phd deletion has been shown to be beneficial on clinical outcome and neuronal survival in a mouse model of intracerebral hemorrhage (Karuppagounder et al., 2016), as well as in a model for stroke (Kunze et al., 2012).

We focused on the hypoxia response of astrocytes, a cell population that is seen as the most relevant CNS subset for the complex metabolic demand of neuronal network activity (Allaman et al., 2011). Astrocytes are essential for oxygen homeostasis in the CNS as they can rapidly detect and react to physiological oxygen fluctuations (Angelova et al., 2015). Furthermore, astrocytes are crucial in regulating lactate, glutamate, water and electrolyte homeostasis, electrical transmission at the tripartite synapse and are the parenchymal part of the blood–brain barrier forming a tight sheet of astrocyte end feet, termed "glia limitans" (GL).

Under most disease conditions, astrocytes change their morphology into "reactive astrocytes," which is a concept that can mean very

different functional phenotypes of astrocytes from securing neuronal integrity to actively contributing to neuroaxonal damage (Escartin et al., 2021). How far reactive astrocytes in pathologic conditions are able to maintain their cell-intrinsic homeostatic functions is unknown. We investigated a transgenic model for astrocyte specific inducible Phd2/Phd3 deletion in experimental autoimmune encephalitis (EAE). EAE, the most utilitarian MS model, is used with concomitant induction of the hypoxia response program in astrocytes during the onset of clinical signs. Our aim was to analyze the role of hypoxia-related mechanisms to chronic inflammatory CNS diseases and to assess the participation of astrocytes.

2 | RESULTS

2.1 | Hypoxia or *Phd2/Phd3* deletion induces astrocyte neuroprotective gene signatures

First, we analyzed astrocytes' ability to react to hypoxia. We used human embryonal stem cell (ESC; H9)-derived induced (H9*i*) astrocytes (Alisch et al., 2021) and mouse wild type (wt) astrocytes. These cultures were generated in media containing fetal cattal serum (FCS), which was removed 3 days before starting the assays to minimize activating effects REF. IF analysis and transcriptomic analysis of activation markers did not show typical signatures of astrocyte reactivity (Escartin et al., 2021; Perriot et al., 2018) at baseline (Figure S1). We exposed cultured astrocytes to mild hypoxia (2.5% O_2; control was kept under normal atmospheric oxygen concentration) for 48 h and checked the expression of genes connected to specific biological pathways (hypoxia response, cell death, neuroprotection) by qPCR. Astrocytes of both species showed a highly significant upregulation of Phd3 (*p.adj.* ≤ 0.0001), Vegfa (*p.adj.* ≤ 0.0001), Bnip3 (H9 *i p.adj.* = 0.0001; mouse *p.adj.* ≤ 0.0001) and Pdk1 (*p.adj.* ≤ 0.0001), (Figure 1a, b). Therefore, astrocytes showed, as expected, a metabolic adaptation to O_2 levels lower than 3% (Shi et al., 2016). We did not detect any sign of induced cell death.

To evaluate the effect of hypoxia-induced transcriptional astrocyte programs in chronic neuroinflammation, we used a conditional deletion model of *Phd2* and *Phd3* restricted to astrocytes. The combined deletion of *Phd2* and *Phd3* has been shown to result in a strong stabilization of HIFα proteins and subsequently an activation of the HIFα-dependent gene program (Minamishima et al., 2009). We crossbred the tamoxifen-inducible astrocyte-specific Aldh1l1-cre^ERT2 and the Phd2^fl/fl and Phd3^fl/fl (cre-inducible) knock-out (ko) mouse strains. Homozygous ko alleles of *Phd2* and *Phd3* will be herein-after termed as Phd2/3-ko, while the wildtype alleles will be referred to as wt.

First, we verified the gene deletion of in vivo tamoxifen induced Phd2/3-ko in FACsorted astrocytes (Figure S2A) according to previously published protocols (Rosiewicz et al., 2020). Genomic DNA analysis identified the Phd2 and Phd3 deletion to be present in Aldh1l1-cre^ERT2; Phd2^fl/fl; Phd3^fl/fl; tdTomato^fl/fl sorted astrocytes
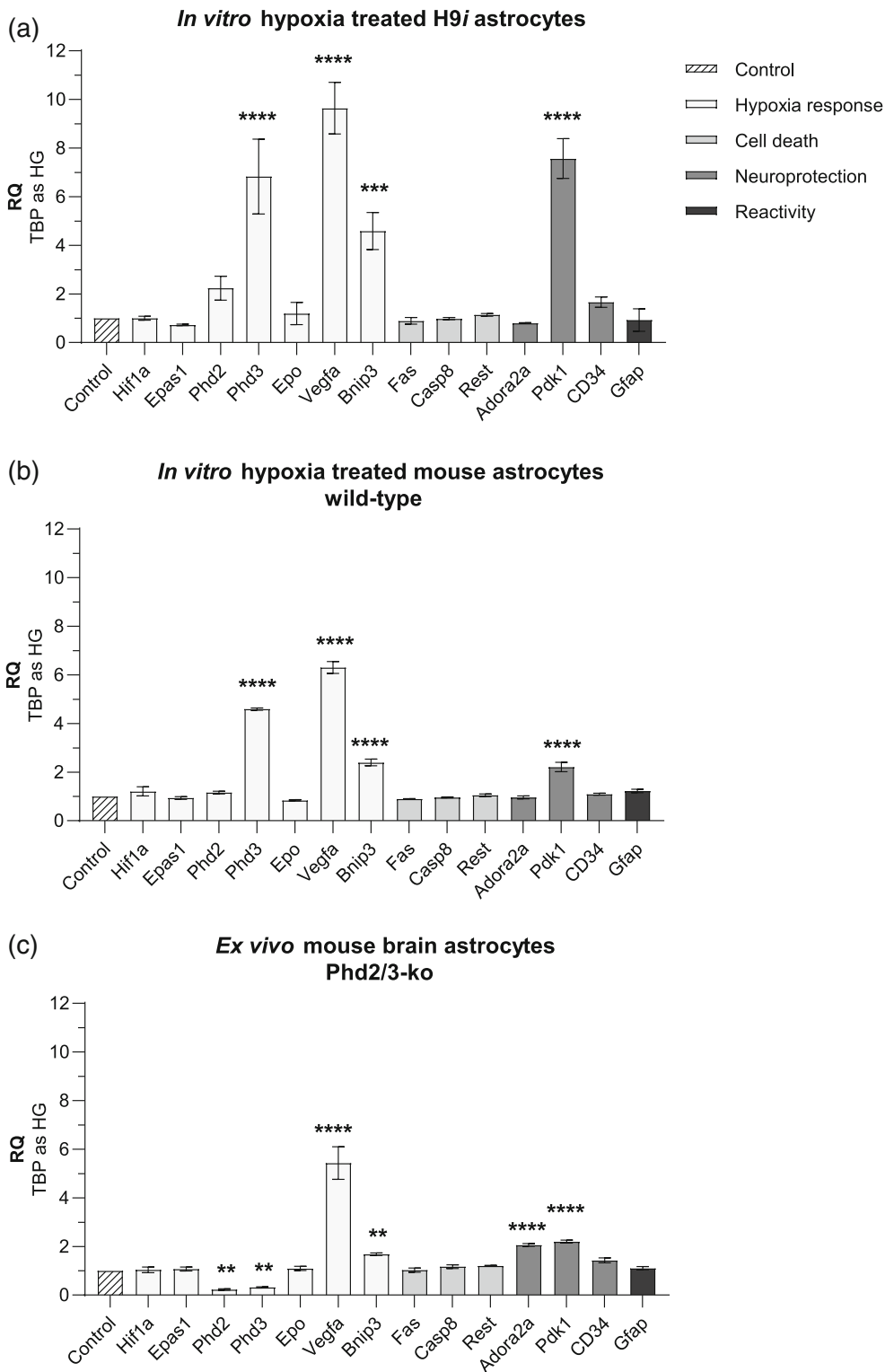
FIGURE 1 Hypoxia related gene expression pattern in astrocytes. (a) H9i astrocytes were treated in vitro with 2.5% O_2 for 48 h. qPCR analysis showed a significant upregulation of hypoxia related genes. (b) Mouse derived astrocytes were treated with 2.5% O_2 for 48 h as well and showed a similar gene expression pattern as H9i astrocytes detected by qPCR. (c) Astrocytes from tamoxifen-treated mice (Aldh1l1-cre[ERT2]; Phd2^{fl/fl}; Phd3^{fl/fl}; tdTomato^{fl/fl}) were FACSorted (CD11b- CD45- ACSA2+ tdTomato+) and analyzed by qPCR. Phd2 and Phd3 expression was significantly downregulated as a consequence of its knock-out, while hypoxia related genes were significantly upregulated. Control bar represents the individual gene expression under normoxia (a + b) or wt (c) condition and served as reference to calculate the relative expression (RQ, relative quantification). TBP served as housekeeping gene (HG); $n = 3$ in all individual experiments per group. Bar graphs are presented as means with SEM. Statistical analysis was performed by using one-way ANOVA with Holm-Sidak's post-hoc test

(Figure S2B). qPCR done on FACsorted astrocytes confirmed a strong downregulation of Phd2 and Phd3 in Phd2/3-ko astrocytes (Figure 1c). Furthermore, these astrocytes showed a similar gene expression pattern to the astrocytes exposed to hypoxia. Simultaneously sorted microglia (CD11b+ CD45[int.]) from the same genotype did not show a deletion of Phd2 and Phd3, supporting the cell population specific induction (Figure S2B).

2.2 | Conditional gene knock out of astrocytic *Phd2* and *Phd3* exacerbates EAE

Animals of both experimental groups (wt and Phd2/3-ko) were age and sex matched. We chose a therapeutic study design with start of Phd2/3-ko induction after onset of clinical symptoms in active EAE (clinical score ≥ 1; all animals reaching this clinical score were treated
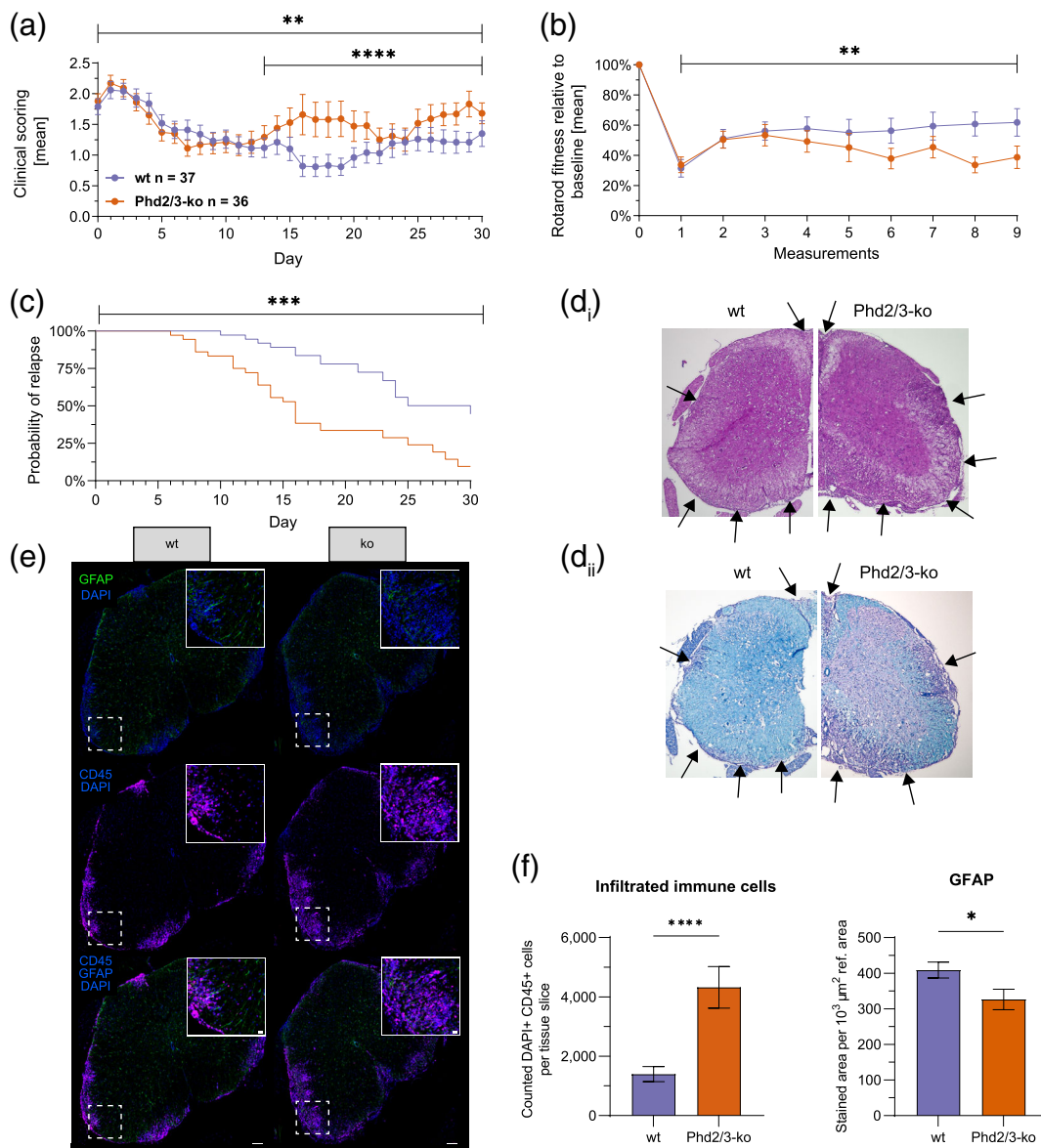
FIGURE 2 Clinical observation and histological analysis revealed a worse EAE outcome for Phd2/3-ko animals. The observed and noted time courses for the mean clinical scoring (a) and Rotarod fitness (b) showed an exacerbated EAE in Phd2/3-ko animals. (c) Calculated probability of getting a relapse (Kaplan–Meier estimator) was significantly increased in the group of Phd2/3-ko animals. (d_i/d_ii) Histological comparison of spinal cord sections (d_i, HE staining; d_ii, LFB staining) demonstrated massive infiltration of peripheral cells in Phd2/3-ko animals (black arrows). (e) Immunofluorescence staining of the spinal cord (wt 26 slices, Phd2/3-ko 19 slices) identified the massively infiltrated peripheral cells as CD45+. Dashed squares indicate the magnified areas located in the upper right corner of every image. White bars in overviews = 100 μm white bars in magnified window = 10 μm. (f) Quantification of DAPI+ CD45+ cells showed strongly increased numbers in Phd2/3-ko animals (left), while the GFAP+ area was decreased (right). Total numbers of animals included in the study: wt $n = 37$, Phd2/3-ko $n = 36$. Experiments with 30 days of observation were performed twice and the experiments with 15 days of observation were performed three times independently. Statistical analysis was performed by using Mann–Whitney U test (a, b, c, f [CD45+ area]), and unpaired t test (F [GFAP+ area]. For (a), (b), (c) we compared all data points covered by a specific time window. Vertical ends of the lines carrying the statistical asterisk symbols indicate which time window was analyzed.

with tamoxifen irrespective of the Phd2 and Phd3 allelic status for four consecutive days). Mice were clinically observed for the following 30 days (Figure 2) or analyzed in depth after 15 days (Figure 3). This late intervention setting has high clinical relevance as it mimics the situation in patients in which treatment after diagnosis of the disease can be initiated.

The analysis of clinical signs documents a highly significant worsening of EAE symptoms for Phd2/3-ko animals. Up to d10 after starting tamoxifen treatment both groups recovered to a mean scoring value of ≤1.25. Starting on d13 after Phd2/3-ko induction a significant deterioration of mean clinical score values to ≥1.5 and higher weight loss (data not shown) were observed in Phd2/3-ko in comparison to
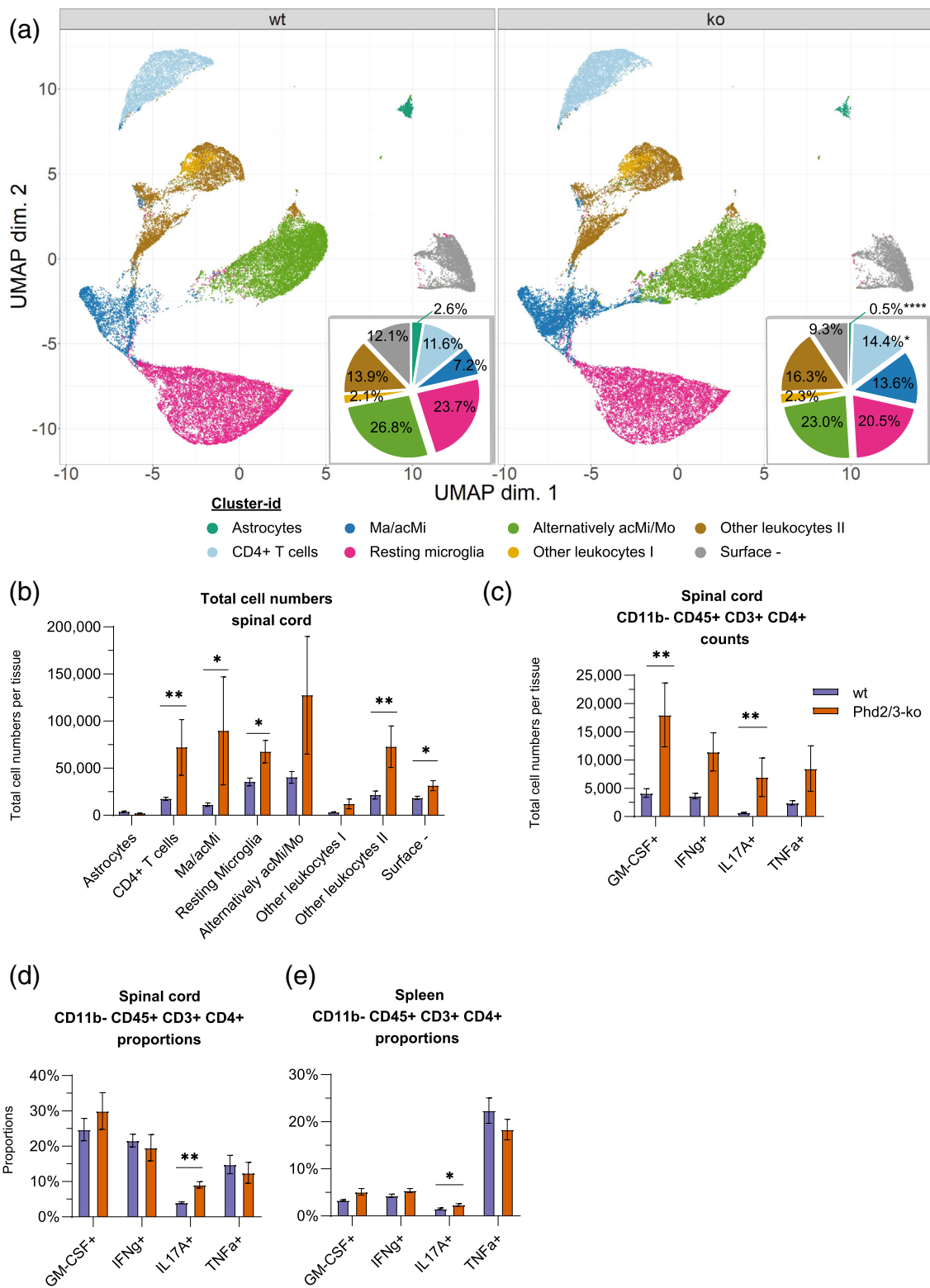
FIGURE 3 Flow cytometric analysis of spinal cord isolated single cells at day 15 post tamoxifen initiation. (a) Computed UMAPs of FACS analysed cells from spinal cords of EAE animals. Proportional distribution of identified clusters is shown in the right corner. FlowSOM was used to define cell clustering and its visualization was done by CATALYST running umap function (UMAP package). Differential analysis of cell cluster abundances was done with diffcyt package. (b) Total cell numbers of each cluster based on cluster proportions and FACS recorded events. (c) Calculated total cell numbers of cytokine producing CD4+ T cells. (d) Proportions of cytokine producing CD4+ T cells. (e) Proportions of cytokine producing CD4+ T cells in control tissue spleen. wt $n = 5$; Phd2/3-ko $n = 5$. Bar graphs shown in (b)–(e) are presented as means with SEM. Statistical analysis of cluster abundances projected by UMAP was done by using the diffcyt-DA-GLMM method. Further tests (for b–e) were done by using Mann–Whitney test and unpaired t test (or Welch's test, if variances where significantly different ($p < .05$))

wt mice (Figure 2a). Phd2/3-ko animals furthermore showed significantly worse Rotarod performance (testing motor endurance) than wt animals in this time period (Figure 2b). We further analyzed the number of mice that developed a relapse (defined as a deterioration of ≥1 clinical scoring point) by using the Kaplan–Meier estimator (Figure 2c). We saw that the probability of developing a relapse was increased for Phd2/3-ko mice. Standard HE and LFB spinal cord sectional staining (day 30 post tamoxifen start) unveiled massive peripheral cell infiltration in Phd2/3-ko animals (Figure 2d$_i$/d$_{ii}$ black arrows). These results, together with the scoring distribution (Figure S2C, S2D), underscore a clear-cut deterioration of EAE outcome for astrocytic Phd2/3-ko animals when induced after onset of clinical signs in EAE. The starting point of clinical deterioration was about 12 days after induction of the knock-out. Mouse phenotypic data are summarized in Table S1. Next, we performed immunofluorescent staining of spinal cord tissue (day 15 after starting tamoxifen) to investigate the pathology in the spinal cord underlying EAE deterioration. Analyzing the number of infiltrating CD45+ cells in the complete white matter (WM), we found that the CD45+ stained area, as marker of peripheral immune cell infiltration, was already highly increased in Phd2/3-ko animals (Figure 2e, f). The GFAP+ area was decreased and so might reflect a lack of reactivity that is typically seen in EAE pathology, though GFAP is not a perfect marker of astrocyte reactivity (Escartin et al., 2021).

2.3 | Phd2/3-KO mice exhibited increased numbers of CNS-infiltrating leukocytes

To decipher the type of inflammatory boost in Phd2/3-ko animals, we studied mice 13–15 days after tamoxifen application and isolated spinal cord and spleen (control tissue). After tissue digestion, single cells were analyzed by flow cytometry. First, we analyzed the different immune-cell populations present in the CNS. To have a genetically encoded astrocyte specific marker implemented as well, we crossed our mouse strain with a fluorescent L10a-eGFP$^{fl/fl}$ mouse strain (Liu et al., 2014) resulting in Aldh1l1-cre^{ERT2}; L10a-eGFP; Phd2$^{fl/fl\ or\ wt/wt}$; Phd3$^{fl/fl\ or\ wt/wt}$. FACS-recorded data were analyzed in an unbiased R-based workflow (Nowicka et al., 2019). By applying FlowSOM (Van Gassen et al., 2015) clustering followed by uniform manifold approximation and projection for dimension reduction (UMAP) (Becht et al., 2018), we classified eight clusters: Aldh1l1-L10a-eGFP (astrocytes), CD45^{hi}CD4+ CD11b- (CD4+ T cells), CD45^{hi}CD11b+ CD86^{hi}MHC-II^{hi} (Macrophages/activated Microglia; Ma/acMi), CD45^{int}CD11b+ MHC-II^{lo}CD11c-(resting Microglia), CD45^{int}CD11b+ CD4+ MHC-II^{int}CD86^{lo} (alternatively activated microglia/monocytes (acMi/Mo)), CD45^{hi}CD11b-CD69+ (other leukocytes I), CD45^{hi}CD11b-CD69- (other leukocytes II), and surface-negative (other CNS cells) (Figures 3a and S3). The proportion of isolated astrocytes was highly reduced in Phd2/3-ko mice (*p.adj* ≤ 0.0001). Inversely, the proportion of CD4+ cells was significantly increased in Phd2/3-ko mice (*p.adj.* = 0.046). CD45^{hi}CD11b+ MHC-II^{hi} (Ma/acMi) co-expressed CD11c+ CD86^{hi} CD69+ and were highly elevated in 3 out of 5 Phd2/3-ko mice. Microglia with a resting phenotype were

identified by CD45^{int}CD11b+ expression and absence of activation markers. There was no statistically significant difference in their proportions. All other clusters (other microglia-like cells, other leukocytes, other CNS cells) were similarly distributed in both groups. A more detailed description of this unbiased FACS analysis is shown in Figure S3.

Since the proportional analysis does not detect synchronized increases of all inflammatory cells in a leukocyte-poor environment, we back-calculated absolute numbers of CNS isolated cells. Based on the cell-cluster proportions and the FACS recorded cell numbers, we calculated the total number of isolated cells of each cell cluster per mouse and genotype (Figure 3b). In Phd2/3-ko mice, the total cell numbers of CD4+ T cells ($p = .008$), Ma/acMi ($p = .032$) cells, resting microglia ($p = .035$), and other leukocytes ($p = .008$) were significantly higher than in wt mice. Although not statistically significant ($p = .085$), there is an indicated trend of reduced astrocyte cell numbers in Phd2/3-ko mice. The confidence intervals for these analyses are shown in Table S4. The actual effect on distinct immune subsets would warrant a larger scaled analysis.

The analysis of the control tissue spleen of the same animals (Figure S4A$_i$) showed that the proportion of CD4+ T cells, inversely to the results in the CNS, was reduced in Phd2/3-ko mice (*p.adj.* = 0.004, Figure S4B). The other cell-cluster proportions showed no statistical differences. The plot for the MDS calculation, the cluster-specific marker expression and the conservative CD11b/CD45 scatter plot all showed clear separation of cell clusters (Figure S4A$_{ii}$, S4C, S4D). In a separate FACS analysis, we investigated cytokine expression after T cell stimulation. For this assay, aliquots of the same CNS and spleen isolated single cell suspensions were taken and plated in mouse medium (MM) and stimulated for 18 h with plate bound anti-CD3 and anti-CD28 antibodies followed by CD4+ T cell and cytokine specific staining and standard FACS analysis (for gating strategy see Figure S5A). We found significantly higher numbers of CNS-isolated GM-CSF ($p = .008$) and IL-17A ($p = .008$) producing CD4+ T cells in Phd2/3 ko mice (Figure 3c). A trend to more IFNg ($p = 0.081$) and TNFa ($p = .021$) producers was also seen. Proportions of IL-17A ($p = .004$) producing CD4+ T cells were increased in the spinal cords and spleens ($p = .027$) of ko mice (Figure 3d, e). Taken together, FACS analysis of spinal cord isolated cells shows in general higher numbers of activated immune cells in Phd2/3-ko mice. Furthermore, within the T cell compartment, significantly higher proportions and cell numbers of pro-inflammatory cytokine-producing T cells suggest an exacerbation of the disease's inflammatory component.

2.4 | Transcriptome analysis reveals regulation of typical hypoxia-dependent genes

To analyze which potential biological pathways could contribute to the inflammatory worsening of EAE in Phd2/3-ko mice we performed an astrocyte specific bulk RNA sequencing analysis using again the Aldh1l1-cre^{ERT2};L10a-eGFP^{fl};Phd2$^{fl/fl\ or\ wt/wt}$;Phd3$^{fl/fl\ or\ wt/wt}$. We used mRNA purification by Translating Ribosome Affinity Purification

(a)

(b)

Heatmap based on all DEGs (60) ko vs wt

(c)

GO terms by PANTHER™
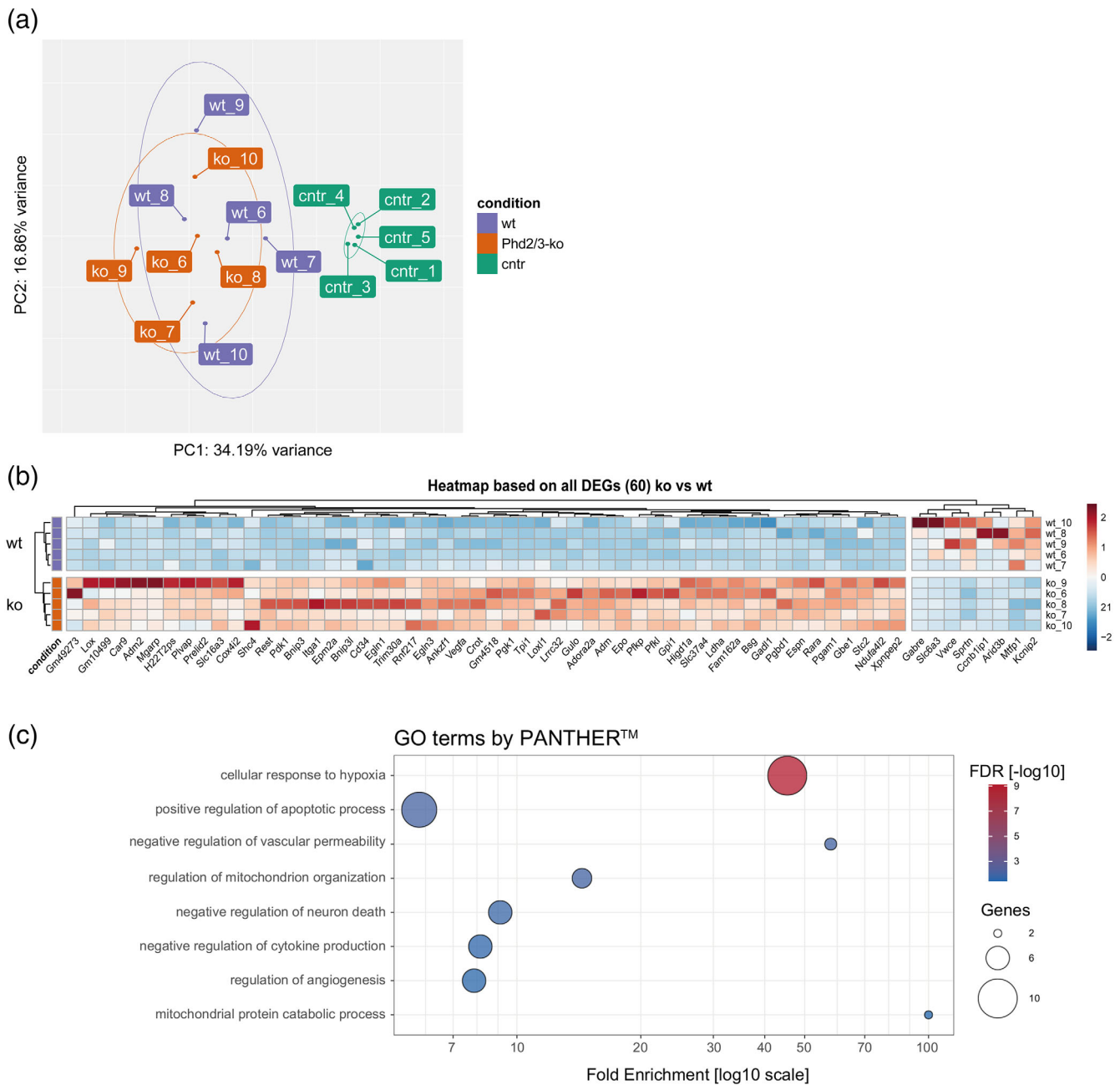
FIGURE 4 Sequencing analysis of actively translated mRNA isolated by TRAP from spinal cord derived astrocytes. (a) PC-Analysis showed a distinct clustering of naïve control animals and EAE animals. (b) Heatmap of re-calculated 60 DEG's between wt and Phd2/3-ko animals excluding naïve control animals from the analysis. (c) By using the PANTHER database we performed a gene enrichment analysis by applying the names of all 60 DEG's. Most relevant statistically significantly enriched GO terms are shown in this bubble plot. The size of bubbles refers to amount of DEG's included in the respective GO term. (d) Gene enrichment analysis by Enrichr database. Most relevant significantly GO terms are shown. Naïve control $n = 5$, wt $n = 5$, Phd2/3-ko $n = 5$

(TRAP) from astrocytes of spinal cord and brain stem as previously described (Rosiewicz et al., 2020). Mice were analyzed 13 to 15 days post tamoxifen treatment start. This time we also included a third experimental group of wt mice which served as non-EAE naïve control (hereafter referred to as control). A first principal component analysis of the whole sequencing data set showed a clear separated clustering of EAE mice (wt and Phd2/3-ko) to the control group (no EAE) (Figure 4a). Comparing total amounts of differentially expressed genes

(DEGs, $p \leq .05$) revealed 94 DEGs in Phd2/3-ko vs. wt, 1275 DEGs in Phd2/3-ko vs. control and 1770 DEGs comparing wt vs. control. This result indicates that there is a dominant effect of EAE related transcriptomic changes in astrocytes (Figure S5B). Furthermore, we detected a general, but not any Phd2/3-ko specific upregulation of inflammatory genes, including the markers for A1 or A2 astrocytes (Figure S5C). Next, we re-analyzed our data excluding the naïve control samples to focus on the Phd2/3-ko effect within EAE. Here, we

(d)
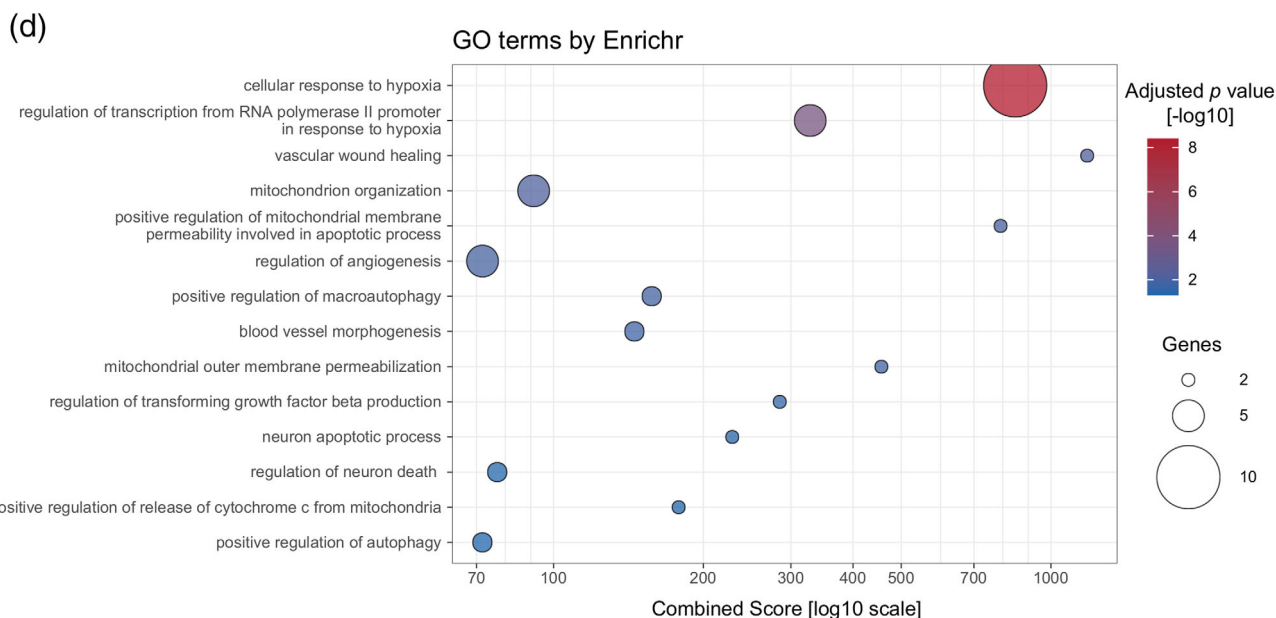
FIGURE 4   (Continued)

found in total 60 DEGs; most were strongly upregulated in Phd2/3-ko EAE animals compared to wt EAE (Figure 4b), but also compared to non-EAE control animals (Figure S6). To understand which particular biological processes could be induced by the conditional ko of *Phd2* and *Phd3*, we performed a GO (Gene Ontology) enrichment analysis using both tools PANTHER™ and Enrichr together with the list of the 60 DEGs. Using PANTHER™, a list of 17 significantly (FDR ≤ 0.05) enriched GO terms was calculated, while Enrichr produced a list of 35 significantly (*adj.p* ≤ .05) enriched GO terms. We shortened these results to the most EAE relevant GO terms. In both datasets, the most significantly enriched GO term was "cellular response to hypoxia" with 10 genes included. Further enriched GO terms identified by PANTHER™ were connected to pro apoptosis, negative vascular permeability, negative regulation of neuronal death, negative cytokine production, regulation of angiogenesis, and mitochondrial organization/catabolic processes (Figure 4c). Enrichr computed similar GO terms, for example angiogenesis, vascular wound healing, apoptosis, neuron apoptotic process, mitochondrial involvement in apoptosis (like cytochrome c release), and autophagy (Figure 4d). We summarized all relevant enriched GO terms into main groups and visualized the expression of their connected genes in respective heatmaps (Figure 5a). Except for Mtfp1, all genes were highly upregulated in Phd2/3-ko astrocytes and this expression pattern very clearly separated all Phd2/3-ko samples from the wt samples with no exception. Interestingly, when comparing the gene lists of these main GO terms inter-group wise, a very conspicuous finding is the fact that most of the genes upregulated in the pathway of "cellular response to hypoxia" can also be found in any other pathway. This state-of-affairs indicates this pathway as a source of a driving force to induce other pathways (Figure 5b). Using only the EAE related DEGs (wt vs control 1770 DEGs), no hypoxia related pathways were significantly enriched

within this gene list (data not shown), suggesting that hypoxia in astrocytes is not a strong feature of EAE in wt conditions at this time point (d15 after disease onset). This observation is in line with findings that expression of HRE dependent genes, such as Vegfa, is a feature rather seen in very acute and serious EAE and is particularly lacking in chronic EAE mice (Roscoe et al., 2009).

2.5 | Astrocytic Phd2/3-ko leads to a reduction of Cx43 gap junctions

The transcriptomic analysis of astrocytes from Phd2/3-ko vs wt animals had yet not explained the phenotype of the mice. Therefore, we analyzed the histopathology to inspect the effect of HRE dependent gene expression in astrocytes on the tissue context in EAE. We quantified ALDH1L1+ area immunofluorescence (IF) in the WM to check for loss of astrocytes upon Phd2/3-ko. However, the analysis showed a similar protein expression in both experimental groups (Figure 6a, b). This finding indicates that there was no reduction in astrocytes in numbers. In line with the transcriptomic results (Figure S7a), we identified a strong upregulation of Vegfa in WM astrocytes of Phd2/3-ko animals (Figure 6a, b), which could be the driving force of the observed effect. Based on previous publications showing that the gap junction (GJ) protein Connexin-43 (Cx43) is internalized due to Vegfa activity (Nimlamool et al., 2015), we analyzed immunofluorescence of this predominant hemichannel for astrocyte syncytial connectivity. We found a strong downregulation of Cx43 IF in Phd2/3-ko animals in NAWM (normal appearing white matter) as well as in acute lesions (Figure 6c, d; confocal analysis in Figure S7C). In contrast, IF of AQP4 – a key molecule of the glia limitans (GL) (Salman et al., 2022)—was unchanged in EAE lesion areas and NAWM in Phd2/-ko compared to wt animals
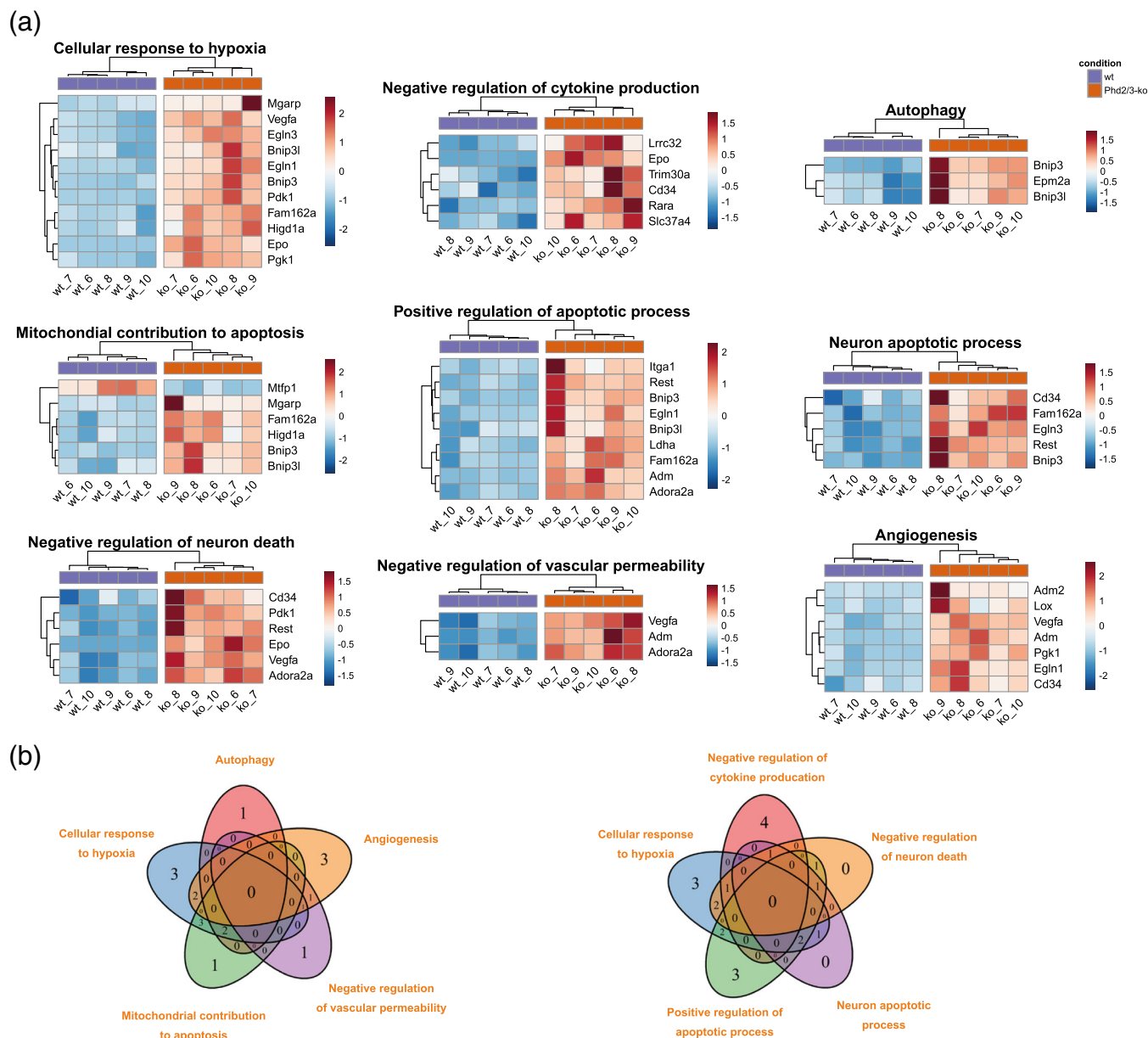
FIGURE 5 Summarized GO terms, their included genes and interconnectivities. A Most relevant GO terms found by PANTHER and Enrichr were summarized and the expression pattern of their included DEG's was shown by a heatmap. (b) Venn Diagrams of the summarized GO terms with the number of shared and not shared genes between the GO terms

(Figure 6e, f; confocal analysis in Figure S8D). Interestingly, the Cx43 (epitope/protein) reduction is not reflected in the transcriptome expression data, which speaks for a post-translational mechanism of this Cx43 loss of immunofluorescence in Phd2/3-ko mice (Figure S7B).

2.6 | Astrocytic Cx43 internalization is induced by Phd2/3-ko driven Vegfa expression

To confirm that the profound overall reduction of Cx43's protein levels in our experiments was a direct consequence of Phd2/3-ko-driven Vegfa upregulation, we first induced an astrocyte-specific

Phd2/3-ko in in vitro cultivated mouse brain slices (chronic hippocampal) from Aldh1l1-cre^{ERT2};L10a-eGFP$^{fl/fl}$;Phd2$^{fl/fl}$;Phd3$^{fl/fl}$ mice. Samples without 4-OH tamoxifen application served as controls. We fixed and stained or directly stained with propidium iodide (PI) the brain slices and analyzed the individual Cx43 proteins by confocal microscopy (Figure 7a), 2 and 12 days post last 4-OH tamoxifen application. We found that Cx43 protein expression gradually decreased after Phd2/3-ko induction, compared to control (Figure 7b; confocal analysis in Figure S8), as shown by significantly reduced volumes and reduced total counts (significant only for day 12) of Cx43 GJs. By performing direct PI staining of the brain slices, we were able to calculate the overall cell survival rates. The survival rates were almost

FIGURE 6 Immuno fluorescence analysis of astrocyte's interconnectivity in the spinal cords of EAE animals 15 days post Tamoxifen treatment start. (a, b) Staining for ALDH1L1 showed no differences between wt and Phd2/3ko animals in the white matter (WM). VEGFA was highly upregulated in the WM of Phd2/3-ko animals. (c, d) Fluorescent microscopy analysis for the gap junction protein Cx43 showed its strong downregulation in normal appearing white matter (NAWM) and acute lesions of Phd2/3-ko animals. (e, f) In contrast, the MFI of astrocyte endfeet located AQP4 showed no difference between wt and Phd2/3-ko animals. Dashed squares in A/C/E indicate magnified areas located in the upper left corner of every image. White bars in overview = 100 μm; white bars in magnified window = 10 μm. B/D/F, bar graphs shown here are presented as means with SEM. Here, statistical analysis was performed by using Mann–Whitney test
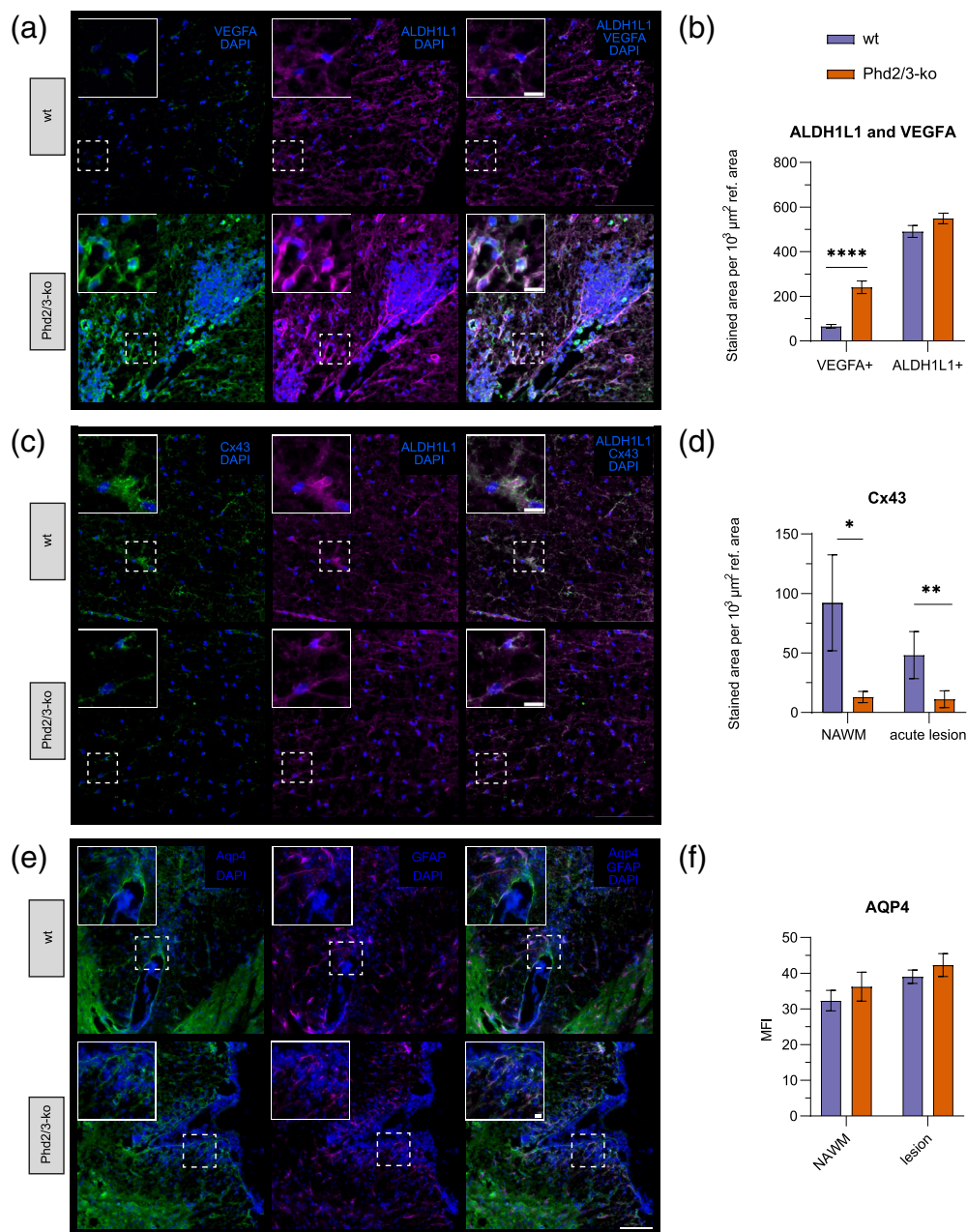
unchanged in both conditions, supporting that neither astrocytic apoptosis nor secondary cell loss of other cell populations is a major event in the astrocytic Phd2/3-ko condition. To investigate the ultrastructural integrity of astrocytes we performed electron microscopy in chronic slice cultures, in which glial-vascular structures have been described as relatively well preserved even weeks after dissection (Chip et al, 2013). Using electron microscopy (EM), we found in both Phd2/3-ko and wt brain slices vascular units with a close ensheathment of astrocytes processes surrounding endothelial cells (Figure 8a). In the perivascular area, astrocyte processes were numerable in both conditions and exhibited similar intracellular EM morphology (Figure 8b). Focusing on contact areas between astrocyte processes, in wt brain slices, there were regularly typical GJ formations between astrocyte processes (Figure 8c). In contrast, in

Phd2/3-ko brain slices GJ formation was rare to absent at contact areas of astrocytes. Thus, the GL is EM-morphologically intact, however the gap junctional astrocyte connectivity is lost upon astrocytic Phd2/3 knock-out.

2.7 | Vegfr blockade inhibits astrocytic HRE-mediated Cx43 downregulation

Since we saw that Cx43 protein downregulation followed after Phd2/3-ko dependent Vegfa upregulation, we tested this hypothesized causality by blocking Vegfr1-3 tyrosine kinases with two different tyrosine kinase inhibitors (TKI) namely fruquintinib (HMPL-013) and vatalanib (PTK787). Fruquintinib has been shown to strongly and
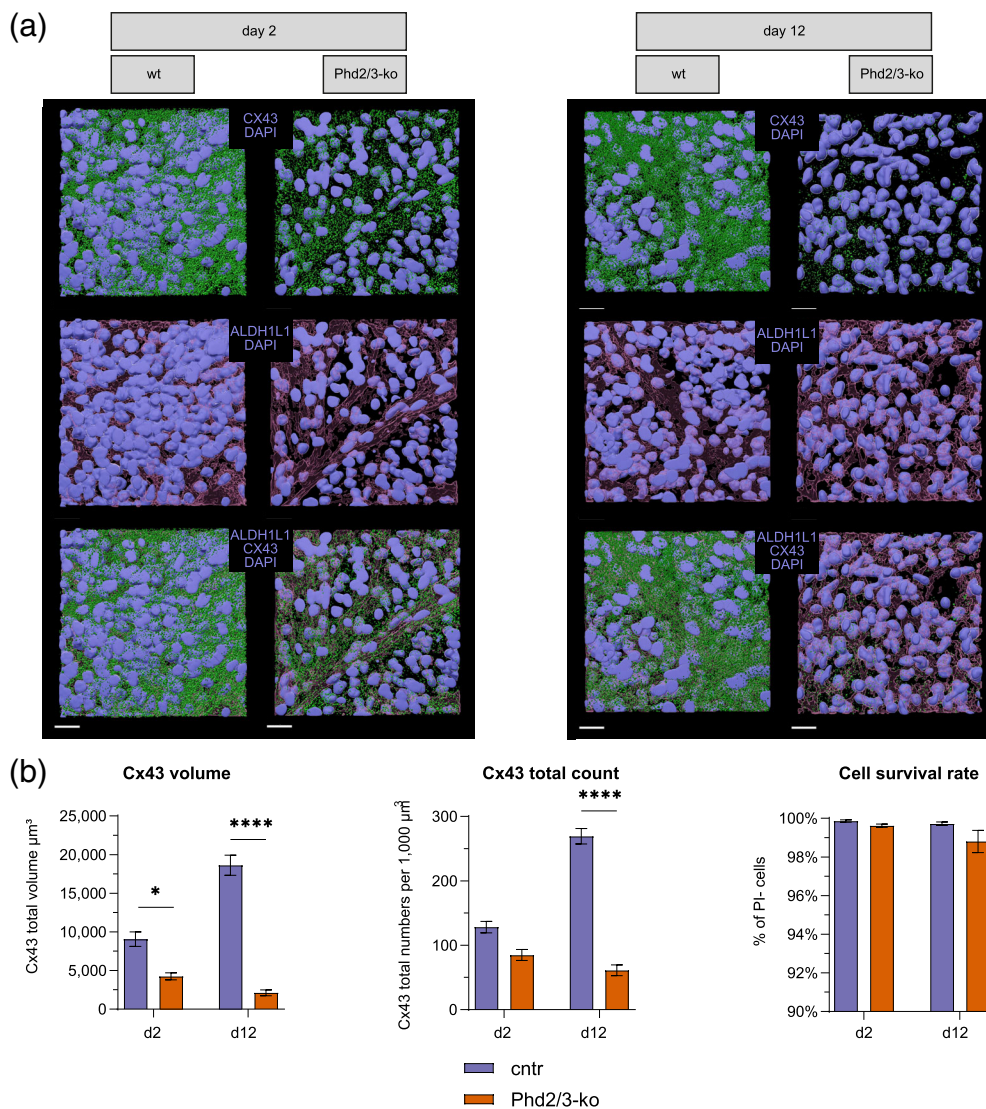
FIGURE 7 Confocal imaging of in vitro cultivated mouse brain slices confirm Cx43 downregulation after Phd2/3-ko induction in Aldh1l1-cre^{ERT2}; L10a-eGFPfl;Phd2$^{fl/fl}$;Phd3$^{fl/fl}$ genotype. (a) 3D reconstructed confocal images of in vitro cultivated mouse brain slices 2 and 12 days after last 4-OH Tamoxifen application. White bars = 20 μm. For d2 7 brain slices wt and 8 brain slices Phd2/3-ko were analyzed. For d12 3 brain slices wt and 4 brain slices Phd2/3-ko were analyzed. In total 23 ROIs per experimental group were analyzed. (b) Quantitative analysis of confocal images showed a strong downregulation of Cx43's volume and total counts. No differences in the cell survival rate was detectable indicating no cytotoxic side effect of 4-OH Tamoxifen application. Bar graphs shown here are presented as means with SEM. Statistical analysis was performed by using Kruskall-Wallis test with Dunn's post-hoc test

specifically inhibit Vegfr1-3 (Sun et al., 2014), while vatalanib effects primarily Vegfr1-3, but also on PDGFR-ß and c-KIT (Wood et al., 2000, p. 787). We applied both TKIs separately on mouse brain slices, which were either Phd2/3-ko induced or treated with Vegfa$_{165}$ peptide. Brain slices were treated three times, every other day. Initial application with TKIs was performed 1 h before first 4-OH tamoxifen or first Vegfa$_{165}$ application to ensure a preliminary inhibition of the Vegfr1-3. A control was treated only with 0.01% DMSO, which corresponded to the remaining concentration in the TKIs. Brain slices were stained 2 days or 12 days after last treatment application for GFAP, Cx43 and for cell viability with PI and analyzed at the confocal microscope (Figure 9a). PI staining showed no increased cell death caused by TKIs (cell survival: control 99.3% ± 0.3; fruquintinib 97.7% ± 0.7; vatalanib 99.5% ± 0.2; Figure 9b; data not shown). Staining for Cx43 revealed a strong significant downregulation of Cx43 GJs in volume and total numbers after Phd2/3-ko induction and Vegfa$_{165}$ application in comparison to control (Figure 9b). This effect was almost completely rescued when fruquintinib or vatalanib was additionally applied. This result confirmed the finding that the downregulation of

Cx43 GJs was a direct consequence of the Phd2/3-ko induced Vegfa upregulation (gene expression and protein level), which could be very potently rescued by blocking the TKs of Vegfr1-3.

3 | DISCUSSION

We investigated the impact of forced HRE-dependent gene induction in astrocytes on the disease course and CNS tissue damage in EAE. Deletion of the oxygen sensors, Phd2/Phd3, in astrocytes after onset of clinical symptoms led to disease exacerbation. Phd2/3-ko astrocytes per se did not exhibit a more pro-inflammatory phenotype than in the Phd2/3 wildtype EAE and even expressed important neuroprotective gene signatures. However, Phd2/3-ko astrocytes lost important traits. For instance, syncytial interconnectivity was influenced, as demonstrated by a strong decrease of hemichannel Cx43 expression and loss of GJs. The HRE-dependent loss of syncytial connectivity led to a higher number of infiltrating immune cells. This response underscores the important homeostatic role of astrocytes' syncytial
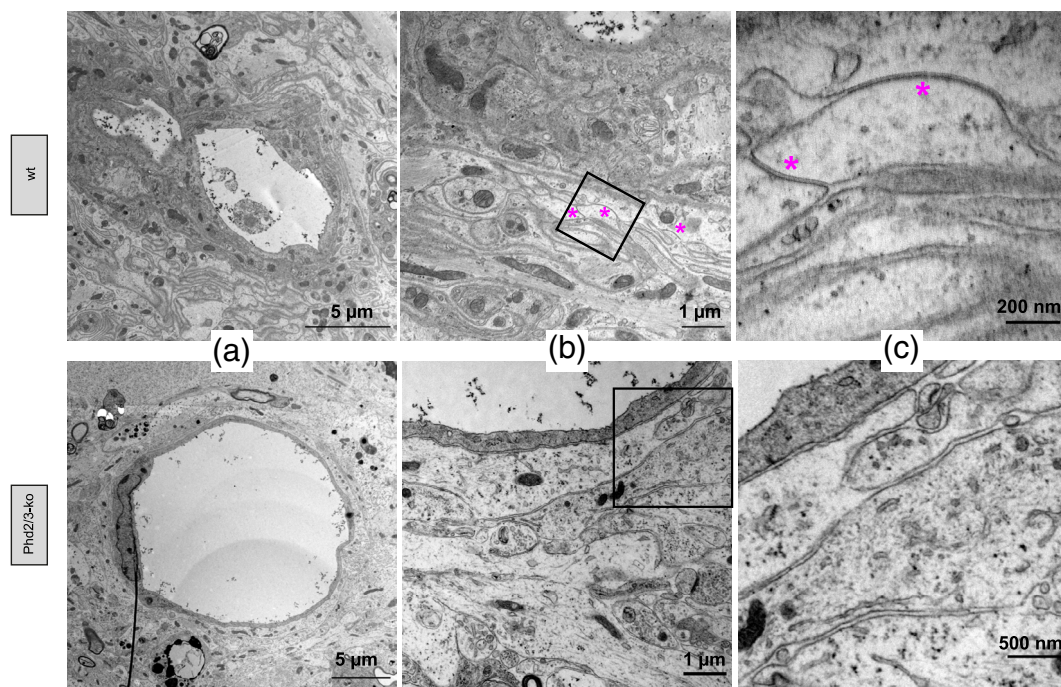
FIGURE 8 Transmission electron microscopy analysis of vessels of chronic hippocampal slice culture. (a) Overview of vessels with intact endothelial cell layer that are enwrapped by astrocytic endfeet. (b) In wt samples areas of astrocyte endfoot-endfoot co-localization showed wide-ranging gap junction formation (magenta asterisks) in every sectional plane. In contrast, Phd2/3-ko samples showed a strong reduction in gap junction formation. Also sparsed punctual tight junctions (green asterisks) were detectable. (c) Corresponding magnified areas to black squares of the middle panels. Here, clearly visible gap junctions at astrocyte endfoot-endfoot zones in wt samples, while completely absent in Phd2/3-ko samples. Three preserved vessels of each experimental condition were found and analyzed. The reduced number of vessels is most likely explainable by the in vitro culture conditions, which lack a constant blood flow

integrity to control inflammatory responses at the interface of the CNS with the blood vessels. Furthermore, our work is the first to show that this in vivo syncytial integrity is disturbed by activation of hypoxia dependent pathways and leads to exacerbated CNS autoimmunity. The role of these processes is undetermined in other CNS diseases.

The idea of exploiting HRE-dependent pathways in inflammatory neurodegeneration derives from the observation of tissue hypoxia in acute EAE lesions (Davies et al., 2013). These investigators also found a correlation between a clinical disease-severity score and degree of tissue hypoxia. Their data support the idea of tissue hypoxia as risk factor for neuroaxonal damage formation in the very acute onset of inflammatory lesions. Several hyperbaric oxygen treatment trials in human MS have been performed; however, these results showed rather anecdotal, transient improvements, and did not support a long-term effect in comparative trials (Bennett & Heard, 2010; Fischer et al., 1983; Wood et al., 1985).

Since evolution has developed a robust program to tackle phases of tissue hypoxia, we hypothesized that boosting the hypoxia response permanently by transgenic activation of HRE pathways might be beneficial for the survival of neurons and the neuroaxonal unit in chronic neuroinflammation. An earlier study showed that Phd2/3-ko leads to stabilizing Hif1α and Hif2α and thus to a strong HRE activation (Minamishima et al., 2009). In vitro, we confirmed

astrocytic expression of HRE dependent genes under hypoxia and upon Phd2/3-ko. We focused on astrocytes as these cells are a central cell population for the metabolic demands of the CNS. Astrocytes have a variety of specific tasks at the BBB, ranging from physically shielding the CNS tissue to securing CNS electrolyte and water homeostasis (Sofroniew & Vinters, 2010). Furthermore, within the CNS parenchyma, astrocytes contribute to providing oxygen and glucose, making them critical supporters of local high-energy demand structures. For instances, the oligodendro-axonal unit and neuronal somata with their dendritic processes and synapses play such a role. In addition, astrocytes are endowed with glutamate transporters to remove potentially neurotoxic glutamate from the extracellular space as well as an enzymatic machinery to degrade glutamate and to protect from reactive oxygen species (ROS).

Animal models have shown that glutamate-mediated neurotoxicity, with high amounts of ROS and mitochondrial impairment, contributes to neuroaxonal damage formation in EAE (Nikić et al., 2011; Siffrin, Radbruch, et al., 2010). Nonetheless, neuronal damage in chronic neuroinflammation is not only dependent on neurotoxic mediators, but also on the capability to counterbalance neuroaxonal damage formation (Schwartz et al., 1999). Several neuroprotective mechanisms have been proposed, including growth factors. Erythropoietin (Epo) is one of these factors with evidence of neuroprotective potential in MS and in animal models (Davies et al., 2013; Sühs
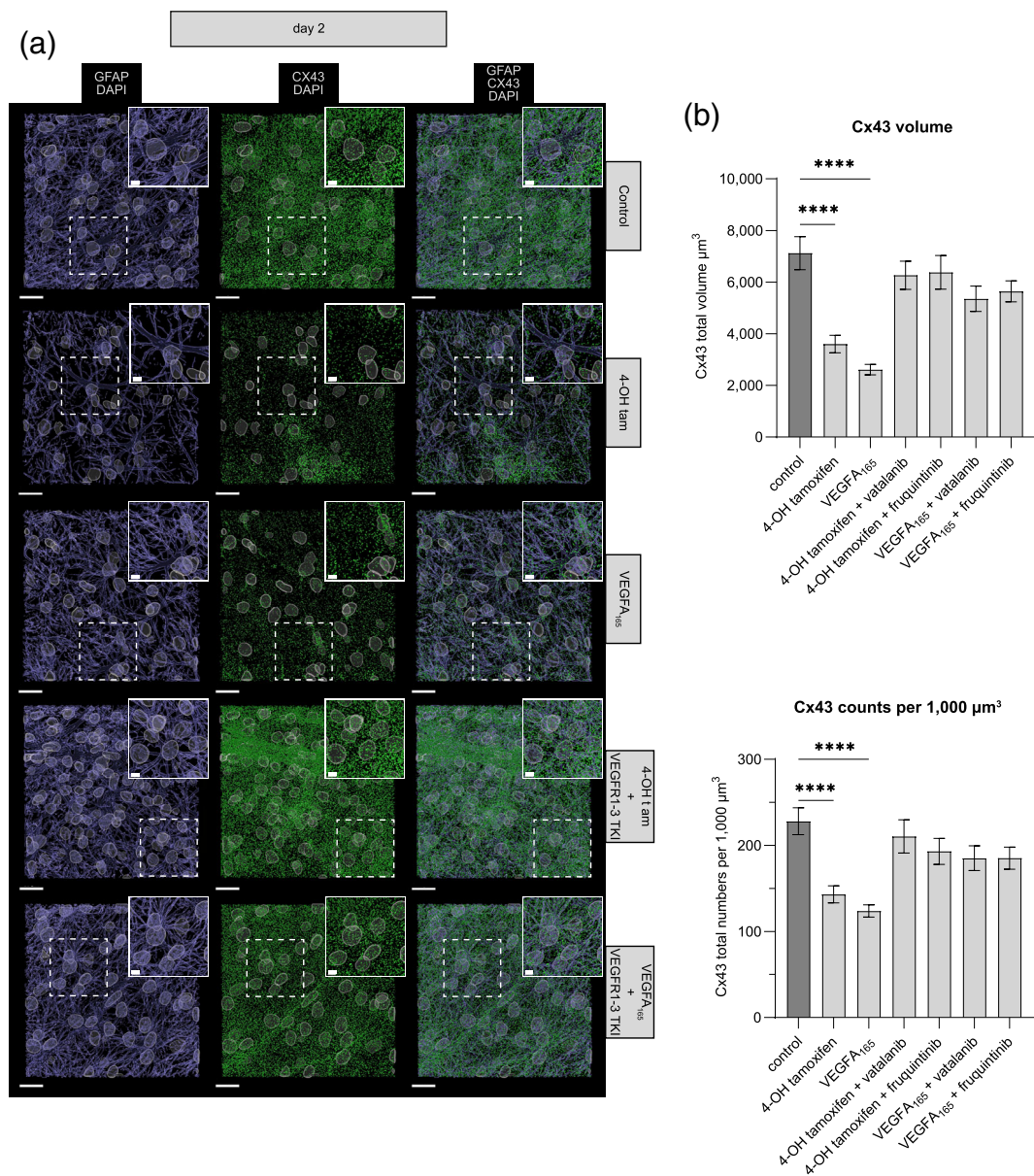
FIGURE 9 Phd2/3-ko induced upregulated VEGFA expression is responsible for Cx43 downregulation confirmed by confocal imaging of in vitro brain slices. (a) 3D confocal images of in vitro cultivated brain slices (Aldh1l1-cre^{ERT2};L10a-eGFP^{fl};Phd2$^{fl/fl}$;Phd3$^{fl/fl}$). First application of fruquintinib or vatalanib was done 1 h before 4-OH-tamoxifen or VEGFA165 was applied. Brain slices were treated 3 times on every other day and were fixed and stained for analysis 2 days after last treatment. One representative confocal image of the conditions 4-OH tamoxifen + fruquintinib and 4-OH tamoxifen + vatalanib is shown as 4-OH tam + VEGFR1-3 TKI. One representative confocal image of the conditions VEGFA165 + fruquintinib and VEGFA165 + vatalanib is shown as VEGFA165 + VEGFR1-3 TKI. Dashed squares indicate magnified areas shown in the upper right corners. White bars in overview = 20 μm, in magnified areas = 5 μm. 5–6 brain slices with up to 26 ROIs in total per experimental group were analyzed. (b) Quantitative analysis of confocal images of Cx43 volumes and total counts. Bar graphs shown here are presented as means with SEM. Statistical analysis was performed by using one-way ANOVA with Sidak's post-hoc test.

et al., 2012). Epo is strongly induced by the transcription factor Hif2α (Chavez et al., 2006). Furthermore, Epo expression in astrocytes has neuroprotective effects for subsequent hypoxic events (Ruscher et al., 2002). Another factor with neuroprotective potential is Vegfa (Jin et al., 2000; Yasuhara et al., 2005). Hypoxia has been shown to increase astrocytic Vegfa expression via Hif1α (Kaur et al., 2006). Our ex vivo transcriptome analysis of astrocytes from Phd2/3-ko EAE mice confirmed strong upregulation of these neuroprotective mediators. Furthermore, the inhibition of neuronal Phds has been shown to reduce ROS production and protect mitochondria from impairment in a model of glutamate mediated oxidative stress (Neitemeier et al., 2016).

In our in vitro experiments we clearly identified HRE dependent gene expression with a potential neuroprotective potential. Therefore, unexpectedly, clinical disease exacerbation was observed in our animals upon astrocytic Phd2/3-ko. In particular, the expression of Vegfa

is a two-edged sword. On the one hand, there is evidence of neuroprotective effects in context of neuroinflammation (Foxton et al., 2013; Froger et al., 2020; Oosthuyse et al., 2001). On the other hand, in a model of constitutive deletion of Vegfa in astrocytes, a beneficial effect on EAE was observed (Argaw et al., 2012). In line with this, blocking Vegf receptor has shown some protective effect in acute EAE (Roscoe et al., 2009), although Vegfa expression is only a transient feature of acute EAE in severely ill animals. We explain our observation in Phd2/3-ko EAE animals by the Vegfa-mediated disruption of astrocyte interconnectivity, which is essential for the control of immune cell entry into the CNS. The syncytial integrity of astrocytes is important for the so-called Glia Limitans (GL), the inner lining of the BBB by astrocytic end-feet. The transmissibility of the brain vessels for peripheral immune cells is dependent not only on the endothelial barrier, but also the presence of an intact GL. In EAE, disrupting astrocytic tight junction protein Claudin-4 led to an increase of immune cell accumulation and worse clinical outcome in an earlier report (Horng et al., 2017). Similarly, the depletion of astrocytes led to an uninhibited entry of peripheral immune cells into the CNS (Voskuhl et al., 2009). The clinical and histopathological phenotype of these rather harsh interventions resembles our results, when we induced HRE driven genes in astrocytes. A limitation of our and the Voskuhl study is that we focused on EAE in the C57BL/6 strain, i.e. we cannot exclude a strain effect of the inbred C57BL/6 mouse strain.

An in vitro study using the oxygen glucose deprivation (OGD) model in astrocytes identified the fact that the phosphorylation of Cx43 led to disassembly of Cx43-based gap junctions (Beckmann et al., 2019). The increasing perivascular Cx43 expression in astrocyte end-feet in postnatal development co-occurs with the maturation of the BBB. However, it is not clear that astrocyte Cx43 disassembly necessarily leads to disease exacerbation. In a toxic MS demyelination model, Cx43 deletion increased remyelination (Li et al., 2020). Nevertheless, the constitutive deletion of Cx43 resulted in a dysfunctional BBB in vivo (Ezan et al., 2012). Interestingly, endothelial tight junctions were still morphologically present and intact, which underscores the idea that the BBB is not only dependent on a tight sealing of the endothelium, but also relies on the syncytial interconnectivity of astrocytes via gap junctions. In how far immune cell entry through the GL is dependent on either Cx43-mediated interactivity or tight junctions or both is currently unknown. Furthermore, it remains unclear, in how far other GJ molecules might also be reduced by astrocytic Phd2/3-ko or compensatorily contribute to the rescue of gap junction activity, as deletion of Cx43 in astrocytes has been shown to result in incomplete blockage of astrocyte coupling (Scemes et al, 1998; Wallraff et al, 2006).

Our data indicate that the complex selection process allowing immune cells to enter the CNS parenchyma includes important steps beyond the transmigration of endothelial cells. Therefore, we believe that the GL is more than a physical barrier for immune cells. The GL is a collective of functionally coupled astrocytes that is severely weakened concerning its immune cell surveillance by HRE induced gap junction disturbance, which leads to severe disease exacerbation in EAE. This interpretation highlights once more the underestimated role of astrocyte physiology in neurologic diseases.

4 | MATERIALS AND METHODS

4.1 | Mice

Approvement for all animal procedures was provided by the "Landesamt für Gesundheit und Soziales Berlin" (license G0056/15). Procedures were in accordance with the European Union Guidelines for care and use of experimental animals. Mouse line Aldh1l1-cre^{ERT2} (Winchenbach et al., 2016) x tdTomato$^{fl/fl}$ was generated and kindly provided by Gesine Saher (Department of Neurogenetics, Max Planck Institute of Experimental Medicine, Göttingen, Germany). B6/J.EGFP-L10a-eGFP (B6;129S4-Gt(ROSA)26Sor$^{tm9(EGFP/Rpl10a)Amc/J}$) mice were purchased from The Jackson Laboratory (USA). Phd2$^{fl/fl}$; Phd3$^{fl/fl}$ mice were kindly provided by Ben Wielockx (Institute for Clinical Chemistry and Laboratory Medicine, Technische Universität Dresden, Germany). Breedings of all animals were performed in house under specific pathogen-free (SPF) conditions in the Max Delbruck Center for Molecular Medicine Berlin.

4.2 | Cell culture of neonatal mouse astrocytes and H9*i* astrocytes

Neonatal primary astrocyte monocultures were prepared from P1-P3 mice and were kindly provided by the working group of Helmut Kettenmann (Max-Delbrück-Centrum für Molekulare Medizin, Berlin, Germany). Procedure was published elsewhere (Ifuku et al., 2020; Lehnardt et al., 2002). Briefly, brains were isolated and cerebellums, olfactory bulbs and meninges were removed. Then, brains were washed 3 times with HBSS and incubated with Trypsin/DNase for 2 min at room temperature. DMEM complete medium (DMEM (gibco), 10% FCS (Sigma-Aldrich), 1% Penicillin/Streptomycin (Pen/Strep), 1% Glutamine (gibco)) was added to stop the reaction followed by trituration in the presence of DNase and washing in DMEM complete medium. Cell suspensions were plated in DMEM complete medium in T75 flasks and cultured for 7 days. Now, medium was changed to DMEM complete supplemented with 30% L929 conditioned medium. After 2 days, T75 flasks were put for 30 min on a horizontal shaker (150 rpm at 37°C) to shake off microglia which were then removed by supernatant aspiration. This was repeated 2 times during the following 4 days. Finally, after treatment with Accutase® the remaining dissociated and washed highly pure astrocytes were frozen and stored in liquid nitrogen. Mouse astrocytes were thawed and plated on Geltrex coated plates and cultured in mouse astrocyte medium (mAM) consisting of DMEM high glucose (gibco), 10% FCS, 1% Pen/Strep and 1× GlutaMAX (gibco).

H9 cells were purchased from Gibco and were finally differentiated to astrocytes (H9*i* astrocytes) by using the methods published by (Alisch et al., 2021). For experiments, previously differentiated and frozen H9*i* astrocytes were thawed and plated on Geltrex coated plates and cultivated in ADM medium (DMEM, 1× GlutaMAX, 1% FCS, 20 ng/mL CNTF (Miltenyi Biotec), 1× N2 Supplement (gibco), 1% Pen/Strep).

In both cases, mouse astrocytes and H9*i* astrocytes, FCS was removed from mAM and ADM 3 days before experiments started due to the reported potential activation of astrocytes by FCS. All experiments were performed in serum-free media.

4.3 | In vitro hypoxia

First, all cell monocultures were kept at 37°C, 5% CO_2 and normal atmospheric oxygen concentration until they reached confluency. Then cells were exposed to mild hypoxia at 2.5% oxygen for 48 h. Control samples stayed at normal atmospheric oxygen concentration. Finally, cells were taken off the incubators washed twice with PBS and lysed directly by applying TRIzol™ (Invitrogen) following RNA purification and cDNA synthesis.

4.4 | Phd2/3 ko induction by tamoxifen application

For in vivo Phd2/3-ko induction tamoxifen (Sigma-Aldrich) was first dissolved in an corn oil: ethanol mix (9:1) at an concentration of 30 mg/mL and then intraperitoneally injected on four consecutive days (3 mg each day).

For in vitro Phd2/3-ko induction in mouse astrocyte monocultures 4-OH tamoxifen (Sigma-Aldrich) was first dissolved in ethanol to 51.6 mM and further diluted in PBS to 2.5 mM stock solution. This stock solution was then added to mAM ending at a final working concentration of 10 μM. Mouse astrocytes were treated 3 times with this working concentration on every other day during regular feeding. Treatment of mouse brain slices was performed in the same way except for the final medium. Here, instead of mAM the mouse brain medium (mBM) was used which is specified in the respective section below.

4.5 | Phd2/3-ko verification and qPCR

gDNA from FACsorted astrocytes was isolated and purified by a standard DNA isolation method. Primer for Phd2: forward CTCACTGACCTACGCCGTGT, reverse GGCAGTGATAACAGGTG-CAA (amplicon 2179 bp wt; 350 bp recombind allele); for Phd3: forward CTCAGACCCCCTAAGTATGT reverse CCACGTTAACTC-TAGAGCCACTGA (amplicon 1228 bp wt; 1000 bp recombind allele).

RNA isolation for qPCR was started by adding TRIzol™, which caused cell lysis following RNA purification by using the Direct-zol RNA microprep® kit from Zymo Research. cDNA synthesis was performed by the High Capacity cDNA Reverse Transcription Kit (Applied Biosystems). Used primer for the qPCR are listed in supplemental Table 2 of the supplements. Tbp was used as a housekeeping gene and the Pfaffl method (Pfaffl, 2001) for the relative quantification (RQ).

4.6 | Experimental autoimmune encephalomyelitis

One week before immunization with MOG_{35-55} mice were trained on the Rotarod (Ugo Basile) for four consecutive days. Here, every mouse was put for 4 min on the Rotarod. The speed of the rod was set to increase slowly reaching a maximum speed after 4 min which marked the end of the run. Every mouse had to complete 3 runs per day in total with a 1 min break in between the runs. After finishing Rotarod training, 3 days later mice were immunized with MOG_{35-55} (125 μg, Charité Universitätsmedizin Berlin) emulsified in complete freund's adjuvant (Sigma-Aldrich) and *Mycobacterium tuberculosis* (H37Ra, 400 μg). Two hours and 24 h post immunization mice were intraperitoneally injected with pertussis toxin (0.3 μg). Mice were screened daily for EAE symptoms, weight change and were put on the Rotarod two times per week with the same setup as during the training phase. The running time was recorded and was always stopped when a mouse fell off the rod. The individual average of the 3 runs per day was calculated. The running times in the pre-EAE onset phase were handled as a reference to the running times post-EAE onset. Mice that started to develop EAE symptoms (EAE score ≥ 1.0) were treated with tamoxifen on four consecutive days irrespective of genotype. Observation periods from EAE onset were 15 and 30 days. Symptoms of EAE were scored as: 0.5, tail paresis; 1.0, tail plegia; 0.5, weak righting reflex; 1.0 hind limp paresis; 2.0 hind limp paralysis; 0.5 forelimb paresis; 1.0, forelimb paralysis. Termination criteria were a total score of 4.0 or a drop in weight below 80% of the initial weight.

4.7 | Histology and immunofluorescence

Mice were first anesthetized with a lethal dose of a ketamine-xylazine mixture (ketamine 320 mg/kg; xylazine 5 mg/kg) and transcardially perfused with 50 mL PBS followed by a perfusion of 30 mL 4% formaldehyde (FA). Then, spinal cord tissue was carefully removed in one whole piece and incubated overnight at 4°C in 2% FA, which was completely replaced with PBS on the next day. Next, tissues were dehydrated by performing a sucrose solution gradient (from 10% to 20% to 30% for 24 h each) and frozen in Tissue Tek® at −80°C. Then, 8 μm thick cryo sections were performed at a cryostat. For the staining, cryo samples were thawed for 30 min at room temperature (RT) followed by a rehydration step (20 min in PBS at RT). An antigen retrieval was performed by placing the samples into pre-heated citrate buffer (10 mM citric acid, pH 6.0) located in a steamer and incubated for 2 min. The steamer was subsequently cooled down by placing it under cold water. Then, samples were blocked for 20 min at RT in blocking buffer (PBS, 1% BSA, 10% NGS, Fc-block (BD Pharmingen)) and washed three times with washing buffer (PBS, 1% BSA). If necessary, a permeabilization was done with 0.4% Triton™ X-100 (Sigma-Aldrich), 1% BSA in PBS for 10 min at RT followed by three times washing. Now, samples were stained with the following primary antibodies overnight at 4°C diluted in staining buffer (PBS, 1% BSA, 2% NGS): CD45 (PE, X-57, rat, Miltenyi Biotec), GFAP (AlexaFluor 488, GA5, mouse, Invitrogen), VEGFA (unconj., C-1, mouse, Santa

Cruz Biotechnology), ALDH1L1 (unconj. poly, rabbit, GeneTex) and Cx43 (unconj. F-7, mouse, Santa Cruz Biotechnology). After three times of washing samples were stained with the following secondary antibodies diluted in staining buffer for 1 h at RT: goat anti-mouse (Invitrogen), goat anti-rabbit (Invitrogen) all conjugated with either AlexaFluor 488, 594 or 647 (depending on antibody panel). After the staining, samples were three times washed, then counter stained with DAPI for 10 min at RT again washed and finally mounted (DAKO). We also performed standard pathological stainings with hematoxylin and eosin (HE) and luxol fast blue (LFB). Mouse brain slices were not frozen but directly fixed in 4% FA (1 h at RT). The procedure of permeabilization, blocking, staining and mounting was the same but with different incubation times. Here, the permeabilization time was 1 h, blocking was 1 h, staining with secondary antibodies was 4 h and counterstaining with DAPI was 1 h. Furthermore, we also checked for cell viability of the brain slices by using propidium iodide (PI, Sigma-Aldrich) staining. We added PI at a concentration of 10 µg/mL to the mBM and incubated for 30 min. Fixation, DAPI staining and mounting was performed as described previously.

Wide-field microscopy was done with the Leica DMI6000B and confocal microscopy with the Leica Stellaris 8 (Cx43 stainings) and Leica SP8 (PI stainings), all in combination with the LAS X software. Confocal imaging of the Cx43 was performed with the 63X oil objective, at a resolution of 1024×1024, $2.4\times$ zoom and in 0.3 µm z-steps. PI stainings were imaged with the $25\times$ objective, $1\times$ zoom, with a resolution of 1024×1024 and in 0.75 µm z-steps.

4.8 | Cell isolation from tissue

Mice were i.p. injected with a lethal dose of anesthetics and transcardially perfused with 50 mL of ice-cold PBS. Brainstem, spinal cord and spleen were removed. The following CNS cell isolation procedure was published in Rosiewicz et al., 2020. Briefly, the CNS tissue was transferred into a petri dish, covered with ice cold D-PBS (Ca^{2+}, Mg^{2+}, glucose, and pyruvate; gibco®), chopped into smaller pieces and transferred into C-tubes® (Miltenyi Biotec, Germany) containing 50 U papain, DNase I (1000 U) and HBSS (gibco). Tissue dissociation and homogenization was performed by putting C-Tubes® on the gentle-MACS® Octo Dissociator with heaters and choosing the program 37C_ABDK_01. Afterwards, ice-cold D-PBS was added to the homogenate and transferred through a 100 µm cell strainer into a 50 mL tube and centrifuged. Then, the supernatant was aspirated, D-PBS and Percoll® were carefully added to the homogenate and a density gradient centrifugation was performed to remove the remaining myelin. After a washing step an erythrolysis was performed followed by a final washing and centrifugation step. Single cells were finally resuspended in a D-PBS/BSA buffer (0.5% BSA, pH 7.2).

Cells from spleen tissues were isolated by a classical mechanical approach. Here, spleen tissue was put on a 100 µm cell strainer, then placed into a petri dish and covered with mouse wash medium (mWM, RPMI 1640 (Gibco)), 1% FCS, 1% Pen/Strep, 1% Hepes (1 M, Gibco). Here, the spleen tissue was meshed through the cell strainer,

transferred into a new 50 mL falcon and filled up with mWM. After a centrifugation at $500\times g$ for 5 min at 4°C, the cell pellet was resuspended and an erythrolysis was performed followed by 2 washing steps and a final single cells resuspension in the D-PBS/BSA buffer.

4.9 | FACSorting of mouse astrocytes for Phd2/3-ko verification

All washing steps were performed at $600\times g$ for 5 min and 4°C. D-PBS/BSA buffer was used as a staining buffer in all steps. Isolated single cells from CNS samples were first Fc-blocked (BD Pharmingen) to prevent unspecific antibody binding. Then, staining with the following primary antibodies was performed for 10 min at 4°C (antibody dilutions were provided by the manufacturer): ACSA-2 (APC, IH3-18A3, Miltenyi Biotec), CD45 (VioGreen, 30F11, Miltenyi Biotec) and CD11b (PerCP, M1/70, Biolegend). After a final washing step cells were resuspended in D-PBS/BSA buffer and analyzed at the BD FACSAria™ II. Astrocytes were identified and sorted as CD11b- CD45-ACSA-2+ tdTomato+. Data visualization was performed with FlowJo™ Software v10.7.1 (BD Life Sciences).

4.10 | Flow cytometry, cell type staining

All washing and staining steps were performed as mentioned for FACSorting of mouse astrocytes. Spleen and CNS cell samples marked for cell type analysis were stained with the following primary antibodies (antibody dilutions were provided by the manufacturer): CD45 (VioGreen, 30F11, Miltenyi Biotec), CD19 (FITC, 6D5, Miltenyi Biotec), CD4 (bio, GK1.5, Biolegend), CD11b (PerCP, M1/70, Biolegend), MHC II (PE, M5/114.15.2, Miltenyi Biotec), CD11c (PE/Cy7, N418, Biolegend), CD86 (APC, PO3, Biolegend), CD69 (APC/Vio770, H1.2F3, Miltenyi Biotec). After a washing step a secondary staining was performed with Streptavidin (BV650, Biolegend). Cells were resuspended in D-PBS/BSA buffer and analyzed at the LSR Fortessa™ (BD).

4.11 | Flow cytometry, ex vivo T cell stimulation and immunostaining

Single cell suspensions marked for cytokine production analysis, were resuspended in mouse medium (MM, WM with 10% FCS, $1\times$ GlutaMAX, 0.01% ß-Mercaptoethanol (50 mM)) and plated on anti-CD3 (BD Pharmingen, clone 145-2C11), anti-CD28 (BD Pharmingen, clone 37.51) coated cell culture plates and incubated overnight followed by immunostaining. Two hours after plating Brefeldin A (Biolegend) was added to every sample. Unstimulated sample aliquots served as controls. After the overnight incubation cells were washed in PBS, Fc-blocked and fixed for 20 min in PFA (2% in PBS) at 4°C. After a washing step in PBS (now $1000\times g$ for 5 min at 4°C) and a washing step in saponin buffer (0.5% Saponin (Carl Roth), 0.5% BSA, pH 7.6) cells

were stained with the following primary antibodies for 20 min at 4°C diluted in saponin buffer: CD11b (PerCP, M1/70, Biolegend), CD45 (VG, 30F11, Miltenyi Biotec), CD4 (bio, GK1.5, Biolegend), CD8 (FITC, 53-6.7, Miltenyi Biotec), CD3 (APC, 145-2C11, BD Bioscience), IFNg (PE/Cy7, XMG1.2, Biolegend), TNFa (APC-Cy7, MP6-XT22, Biolegend), IL-17A (eFluor450, eBio17B7, eBioscience) and GM-CSF (PE, MP1-22E9, Invitrogen). Cells were washed and stained with the secondary antibody Streptavidin (BV650, Biolegend) diluted in saponin buffer. After two washing steps (first in saponin buffer, second in D-PBS/BSA buffer) cells were resuspended in D-PBS/BSA buffer and taken for analysis at the LSR Fortessa™ (BD).

4.12 | Unbiased analysis of flow cytometry data

To analyze the CNS isolated cell types we chose an unbiased and R based approach which was published originally for CyTOF (cytometry by time of light) data by (Nowicka et al., 2019). This excellent workflow can be also adapted for flow cytometry data. Raw data was pre-processed in FlowJo and doublets were excluded. Calculated cell cluster by FlowSOM (Van Gassen et al., 2015) and their relationships visualized by uniform manifold approximation and projection for dimension reduction (UMAP) (Becht et al., 2018) were back tested by performing multidimensional scaling (MDS) plots. Using diffcyt (Weber et al., 2019) package we tested for differential abundances of clusters.

4.13 | mRNA isolation from mouse astrocytes and sequencing

For a detailed protocol please refer to Heiman et al., 2014; Rosiewicz et al., 2020. All steps were done on ice. Briefly explained, mouse spinal cord and brain stem (Aldh1l1-cre^{ERT2}; L10a-eGFP; Phd2$^{fl/fl \text{ or } wt/wt}$; Phd3$^{fl/fl \text{ or } wt/wt}$) were collected from lethally anesthetized and transcardially perfused mice and were homogenized on ice. After different washing steps an immunolabeling of the mRNA carrying L10a-eGFP tagged ribosomes was performed by using streptavidin beads coated with anti-eGFP antibodies (Htz-19C8 and Htz-19F7, Memorial Sloan Kettering Cancer Center). Finally enriched L10a-eGFP tagged ribosomes were treated with TRIzol™® to achieve a release of the bound mRNA, which was then purified by using the Direct-zol RNA microprep® Kit from Zymo Research. Purified samples were send to the Genomics Platforms of the Max Delbrück Center for Molecular Medicine in Berlin, Germany. Library preparation was done with Illumina TruSeq stranded mRNA library kit. Sequencing was performed on the HiSeq 4000 System.

4.14 | Processing of sequencing data

First, sequencing data were checked for rRNA content, which was then filtered-out by using SortMeRNA (Kopylova et al., 2012). Then,

by using the published pipeline by (Pertea et al., 2016) we checked the rRNA depleted data of Aldh1l1-cre^{ERT2}; L10a-eGFP; Phd2$^{fl/fl}$; Phd3$^{fl/fl}$ mice for the correct presence of recombined Phd2 and Phd3 transcript variants (Aldh1l1-cre^{ERT2}; L10a-eGFP; Phd2$^{wt/wt}$; Phd3$^{wt/wt}$ served as control). Phd2/3-ko samples not showing the recombined transcript variants of Phd2 and Phd3 were excluded from this study. This cleaned-up sequencing data was then taken for gene expression quantification done by Salmon (Patro et al., 2017) followed by its statistical analysis by the R based package DESeq2 (Love et al., 2014). GO enrichment analysis was done using the tools of Enrichr (Kuleshov et al., 2016) and PANTHER™ (Mi et al., 2013). The latter mentioned is integrated on Gene Ontology (Ashburner et al., 2000; The Gene Ontology Consortium et al., 2021).

4.15 | In vitro mouse brain slices culture

Organotypic brain culture slices were prepared from postnatal day 5 Aldh1l1-cre^{ERT2}; L10a-eGFP; Phd2$^{fl/fl}$; Phd3$^{fl/fl}$ and Bl6 wild-type mice as a control group. Animals were sacrificed by decapitation using a quick cut with large scissors at the level of the foramen magnum. The skull was opened with fine scissors and brain was removed carefully using small spatulas. Hippocampi were extracted under a dissecting microscope in a laminar flow hood and carefully dissected to be cultured using razor blades and spatulas with polished edges. After freeing hippocampi from blood vessels and meninges, 400 μm thick slices were cut with McIlwain-type tissue chopper. Slices were transferred to a 30 mm petri dish using a cut, fire-polished Pasteur pipet filled with ice-cold dissecting medium (1% L-glutamine in minimum essential medium (MEM) 1×, gibco). Under the dissecting microscope, the best slices with intact morphology, clear cell body layer and homogeneous thickness were selected, aspirated into a cut, fire-polished Pasteur pipet and transferred to 0.4 μm semi-porous membrane inserts (Millipore). The excess medium was removed. Brain slices were maintained in culture for 2 weeks in mBM, containing 50% MEM 1× (gibco), 25% heat inactivated horse serum, 25% HBSS, 13 mM HEPES, 1% Pen/Strep, 20% glucose (35 mM), 2% B27 supplement (gibco) and incubated at 37°C, 95% humidity rate, 5% CO_2. The nutrient medium was replaced every 2 days. 4-OH tamoxifen was applied as described above. 2 days and 12 days after last 4-OH tamoxifen application brain slices were fixed, stained and microscoped.

4.16 | In vitro Vegfa inhibition

Both Vegfr tyrosine kinase inhibitors (TKI) fruquintinib (HMPL-013) and vatalanib (PTK787) (Raybiotech, 10 mM in 1 mL DMSO) were purchased at Hölzel Diagnostika Handels GmbH, Germany and were diluted to a final concentration of 100 nM/mL in mBM. Brain slices were treated 3 times every 2 days, while the first application was considered to be given 1 h before first 4-OH tamoxifen or VEGF$_{165}$ (final concentration 100 ng/mL, recombinant murine, PeproTech) was applied. Two days after last application, brain slices were fixed,

stained and analyzed by confocal microscopy. Application with 0.01% DMSO served as control.

4.17 | Electron microscopy

Chronic hippocampal slice cultures were fixed by immersion in 2% (w/v) paraformaldehyde plus 2.5% (v/v) glutaraldehyde in 0.1 M phosphate buffer for 3 h at room temperature (RT). Samples were post-fixed with 1% (v/v) osmium tetroxide for 2 hours at RT. After dehydration through a graded series of ethanol, embedding was done in PolyBed® 812 resin [Polysciences, Germany]. Ultrathin resin sections (60–80 nm) were stained with uranyl acetate and lead citrate, and imaged at 80 kV with a transmission electron microscope [Morgagni, FEI, The Netherlands]. Acquisition was done with the Morada CCD camera using iTEM software [Emsis GmbH, Germany].

4.18 | Image analysis of microscopy data

Immunofluorescence wide-field microscopy data were analyzed with ImageJ (Schneider et al., 2012) and confocal microscopy data of Cx43 stainings with Imaris (Oxford Instruments Technologies). To quantify total number of dead cells (PI punctae) over the total number of cells in a given mouse brain slice (DAPI punctae) 3D object counter plugin (Bolte & Cordelières, 2006) on ImageJ was used.

4.19 | Statistics

Statistical analysis of mRNA sequencing data and flow cytometry data (only cell type analysis) were performed with the respective R packages. Clinical data, qPCR data, immunofluorescence data, data of the CD4+ T cell cytokine expression assay were statistically analyzed using GraphPad Prism. If data was normally distributed, then either the unpaired t test with/without Welch's correction or one-way ANOVA with a post-hoc test was performed. Regarding not normally distributed data, the Mann–Whitney U test or Kruskall–Wallis test including a post-hoc test was performed. Regarding test strategy the following post-hoc tests were used: Holm-Sidak's, Dunn's, Dunnett T3. Statistical significance was defined as $*p \leq .05$; $**p \leq .01$, $***p \leq .001$, $****p \leq .0001$.

AUTHOR CONTRIBUTIONS

Volker Siffrin and Kamil Sebastian Rosiewicz designed the research project and the experiments and wrote the manuscript. Friedemann Paul, Marlen Alisch, and Jessy Chen advised on and supported experiments and data analysis. Ben Wielockx provided transgenic mice, critical advice on the research outline and the manuscript. Helena Radbruch advised on, supported and performed immunofluorescence experiments. Marlen Alisch, Julia Ucar, Tadhg Crowley, Janis Kerkering, Bakhrom Muinjonov, Séverine Kunz, René Jüttner, and Kamil Sebastian Rosiewicz performed experiments.

CONFLICT OF INTEREST STATEMENT

VS has received research funding from Novartis Pharma AG, Alexion Pharmaceuticals and Roche Pharma AG. MA has received research funding from Novartis Pharma AG. FP is a co-founder and holds shares in technology start-up Nocturne GmbH, receives honoraria for lecturing and travel expenses for attending meetings from Guthy Jackson Foundation, Bayer, Biogen, Merck Serono, Sanofi Genzyme, Novartis, Alexion, Viela Bio, Roche, UCB, Mitsubishi Tanabe and Celgene. His research is funded by the German Ministry for Education and Research (BMBF), Deutsche Forschungsgemeinschaft (DFG), Einstein Foundation, Guthy Jackson Charitable Foundation, EU FP7 Framework Program, Biogen, Genzyme, Merck Serono, Novartis, Bayer, Alexion, Roche, Parexel and Almirall.

DATA AVAILABILITY STATEMENT

The transcriptomics data from RNA sequencing experiments (Figures 4, 5b, c, S5, S6 and S7A, B) are available at Dryad (doi:10.5061/dryad.jwstqjqdb). All other data supporting the findings from this study are available from the authors upon reasonable request.

ORCID

Volker Siffrin 🔘 https://orcid.org/0000-0002-1532-2868

REFERENCES

Alisch, M., Kerkering, J., Crowley, T., Rosiewicz, K., Paul, F., & Siffrin, V. (2021). Identification of the gliogenic state of human neural stem cells to optimize in vitro astrocyte differentiation. _Journal of Neuroscience Methods_, _361_, 109284.

Allaman, I., Bélanger, M., & Magistretti, P. J. (2011). Astrocyte–neuron metabolic relationships: For better and for worse. *Trends in Neurosciences*, *34*, 76–87.

Angelova, P. R., Kasymov, V., Christie, I., Sheikhbahaei, S., Turovsky, E., Marina, N., Korsak, A., Zwicker, J., Teschemacher, A. G., Ackland, G. L., Funk, G. D., Kasparov, S., Abramov, A. Y., & Gourine, A. V. (2015). Functional oxygen sensitivity of astrocytes. *The Journal of Neuroscience*, *35*, 10460–10473.

Argaw, A. T., Asp, L., Zhang, J., Navrazhina, K., Pham, T., Mariani, J. N., Mahase, S., Dutta, D. J., Seto, J., Kramer, E. G., Ferrara, N., Sofroniew, M. V., & John, G. R. (2012). Astrocyte-derived VEGF-A drives blood-brain barrier disruption in CNS inflammatory disease. *The Journal of Clinical Investigation*, *122*, 2454–2468.

Ashburner, M., Ball, C. A., Blake, J. A., Botstein, D., Butler, H., Cherry, J. M., Davis, A. P., Dolinski, K., Dwight, S. S., Eppig, J. T., Harris, M. A., Hill, D. P., Issel-Tarver, L., Kasarskis, A., Lewis, S., Matese, J. C., Richardson, J. E., Ringwald, M., Rubin, G. M., & Sherlock, G. (2000). Gene ontology: Tool for the unification of biology. *Nature Genetics*, *25*, 25–29.

Becht, E., McInnes, L., Healy, J., Dutertre, C.-A., Kwok, I. W. H., Ng, L. G., Ginhoux, F., & Newell, E. W. (2018). Dimensionality reduction for visualizing single-cell data using UMAP. *Nature Biotechnology*, *37*, 38–44.

Beckmann, A., Grißmer, A., Wolf, S., Recktenwald, J., & Meier, C. (2019). Oxygen-glucose deprivation in mouse astrocytes is associated with ultrastructural changes in Connexin 43 gap junctions. *Neuroscience*, *397*, 67–79.

Bennett, M., & Heard, R. (2010). Hyperbaric oxygen therapy for multiple sclerosis. *CNS Neuroscience & Therapeutics*, *16*, 115–124.

Berra, E., Benizri, E., Ginouvès, A., Volmat, V., Roux, D., & Pouysségur, J. (2003). HIF prolyl-hydroxylase 2 is the key oxygen sensor setting low steady-state levels of HIF-1alpha in normoxia. *The EMBO Journal*, *22*, 4082–4090.

Bolte, S., & Cordelières, F. P. (2006). A guided tour into subcellular colocalization analysis in light microscopy. *Journal of Microscopy*, *224*, 213–232.

Chavez, J. C., Baranova, O., Lin, J., & Pichiule, P. (2006). The transcriptional activator hypoxia inducible factor 2 (HIF-2/EPAS-1) regulates the oxygen-dependent expression of erythropoietin in cortical astrocytes. *Journal of Neuroscience: The Official Journal of the Society for Neuroscience*, *26*, 9471–9481.

Chip, S., Nitsch, C., Wellmann, S., Kapfhammer, J.P. (2013). Subfield-specific neurovascular remodeling in the entorhino-hippocampal-organotypic slice culture as a response to oxygen-glucose deprivation and excitotoxic cell death. *J Cereb Blood Flow Metab*, *33*, 508–518.

Correia, S. C., & Moreira, P. I. (2010). Hypoxia-inducible factor 1: A new hope to counteract neurodegeneration? *Journal of Neurochemistry*, *112*, 1–12.

Davies, A. L., Desai, R. A., Bloomfield, P. S., McIntosh, P. R., Chapple, K. J., Linington, C., Fairless, R., Diem, R., Kasti, M., Murphy, M. P., & Smith, K. J. (2013). Neurological deficits caused by tissue hypoxia in neuroinflammatory disease. *Annals of Neurology*, *74*, 815–825.

Escartin, C., Galea, E., Lakatos, A., O'Callaghan, J. P., Petzold, G. C., Serrano-Pozo, A., Steinhäuser, C., Volterra, A., Carmignoto, G., Agarwal, A., Allen, N. J., Araque, A., Barbeito, L., Barzilai, A., Bergles, D. E., Bonvento, G., Butt, A. M., Chen, W. T., Cohen-Salmon, M., … Verkhratsky, A. (2021). Reactive astrocyte nomenclature, definitions, and future directions. *Nature Neuroscience*, *24*, 312–325.

Ezan, P., André, P., Cisternino, S., Saubaméa, B., Boulay, A.-C., Doutremer, S., Thomas, M.-A., Quench'du, N., Giaume, C., & Cohen-Salmon, M. (2012). Deletion of astroglial connexins weakens the blood–brain barrier. *Journal of Cerebral Blood Flow and Metabolism*, *32*, 1457–1467.

Fischer, B. H., Marks, M., & Reich, T. (1983). Hyperbaric-oxygen treatment of multiple sclerosis. A randomized, placebo-controlled, double-blind study. *The New England Journal of Medicine*, *308*, 181–186.

Foxton, R. H., Finkelstein, A., Vijay, S., Dahlmann-Noor, A., Khaw, P. T., Morgan, J. E., Shima, D. T., & Ng, Y.-S. (2013). VEGF-A is necessary and sufficient for retinal neuroprotection in models of experimental glaucoma. *The American Journal of Pathology*, *182*, 1379–1390.

Froger, N., Matonti, F., Roubeix, C., Forster, V., Ivkovic, I., Brunel, N., Baudouin, C., Sahel, J.-A., & Picaud, S. (2020). VEGF is an autocrine/paracrine neuroprotective factor for injured retinal ganglion neurons. *Scientific Reports*, *10*, 12409.

Heiman, M., Kulicke, R., Fenster, R. J., Greengard, P., & Heintz, N. (2014). Cell-type-specific mRNA purification by translating ribosome affinity purification (TRAP). *Nature Protocols*, *9*, 1282–1291.

Horng, S., Therattil, A., Moyon, S., Gordon, A., Kim, K., Argaw, A. T., Hara, Y., Mariani, J. N., Sawai, S., Flodby, P., Crandall, E. D., Borok, Z., Sofroniew, M. V., Chapouly, C., & John, G. R. (2017). Astrocytic tight junctions control inflammatory CNS lesion pathogenesis. *The Journal of Clinical Investigation*, *127*, 3136–3151.

Ifuku, M., Hinkelmann, L., Kuhrt, L. D., Efe, I. E., Kumbol, V., Buonfiglioli, A., Krüger, C., Jordan, P., Fulde, M., Noda, M., Kettenmann, H., & Lehnardt, S. (2020). Activation of toll-like receptor 5 in microglia modulates their function and triggers neuronal injury. *Acta Neuropathologica Communications*, *8*, 159.

Jin, K. L., Mao, X. O., & Greenberg, D. A. (2000). Vascular endothelial growth factor: Direct neuroprotective effect in in vitro ischemia. *Proceedings of the National Academy of Sciences of the United States of America*, *97*, 10242–10247.

Jonz, M. G., Buck, L. T., Perry, S. F., Schwerte, T., & Zaccone, G. (2016). Sensing and surviving hypoxia in vertebrates. *Annals of the new York Academy of Sciences*, *1365*, 43–58.

Karuppagounder, S. S., Alim, I., Khim, S. J., Bourassa, M. W., Sleiman, S. F., John, R., Thinnes, C. C., Yeh, T.-L., Demetriades, M., Neitemeier, S., Cruz, D., Gazaryan, I., Killilea, D. W., Morgenstern, L., Xi, G., Keep, R. F., Schallert, T., Tappero, R. V., Zhong, J., … Ratan, R. R. (2016). Therapeutic targeting of oxygen-sensing prolyl hydroxylases abrogates ATF4-dependent neuronal death and improves outcomes after brain hemorrhage in several rodent models. *Science Translational Medicine*, *8*, 328ra29.

Kaur, C., Sivakumar, V., Zhang, Y., & Ling, E. A. (2006). Hypoxia-induced astrocytic reaction and increased vascular permeability in the rat cerebellum. *Glia*, *54*, 826–839.

Kopylova, E., Noé, L., & Touzet, H. (2012). SortMeRNA: Fast and accurate filtering of ribosomal RNAs in metatranscriptomic data. *Bioinformatics*, *28*, 3211–3217.

Korovina, I., Neuwirth, A., Sprott, D., Weber, S., Sardar Pasha, S. P. B., Gercken, B., Breier, G., El-Armouche, A., Deussen, A., Karl, M. O., Wielockx, B., Chavakis, T., & Ameln, A. K.-v. (2019). Hematopoietic hypoxia-inducible factor 2α deficiency ameliorates pathological retinal neovascularization via modulation of endothelial cell apoptosis. *The FASEB Journal*, *33*, 1758–1770.

Kuleshov, M. V., Jones, M. R., Rouillard, A. D., Fernandez, N. F., Duan, Q., Wang, Z., Koplev, S., Jenkins, S. L., Jagodnik, K. M., Lachmann, A., McDermott, M. G., Monteiro, C. D., Gundersen, G. W., & Ma'ayan, A. (2016). Enrichr: A comprehensive gene set enrichment analysis web server 2016 update. *Nucleic Acids Research*, *44*, W90–W97.

Kunze, R., Zhou, W., Veltkamp, R., Wielockx, B., Breier, G., & Marti, H. H. (2012). Neuron-specific prolyl-4-hydroxylase domain 2 knockout reduces brain injury after transient cerebral ischemia. *Stroke*, *43*, 2748–2756.

Lehnardt, S., Lachance, C., Patrizi, S., Lefebvre, S., Follett, P. L., Jensen, F. E., Rosenberg, P. A., Volpe, J. J., & Vartanian, T. (2002). The toll-like receptor TLR4 is necessary for lipopolysaccharide-induced oligodendrocyte injury in the CNS. *The Journal of Neuroscience*, *22*, 2478–2486.

Li, T., Niu, J., Yu, G., Ezan, P., Yi, C., Wang, X., Koulakoff, A., Gao, X., Chen, X., Sáez, J. C., Giaume, C., & Xiao, L. (2020). Connexin 43 deletion in astrocytes promotes CNS remyelination by modulating local inflammation. *Glia*, *68*, 1201–1212.

Liu, J., Krautzberger, A. M., Sui, S. H., Hofmann, O. M., Chen, Y., Baetscher, M., Grgic, I., Kumar, S., Humphreys, B. D., Humphreys, B., Hide, W. A., & McMahon, A. P. (2014). Cell-specific translational profiling in acute kidney injury. *The Journal of Clinical Investigation*, *124*, 1242–1254.

Love, M. I., Huber, W., & Anders, S. (2014). Moderated estimation of fold change and dispersion for RNA-seq data with DESeq2. *Genome Biology*, *15*, 550.

Mi, H., Muruganujan, A., Casagrande, J. T., & Thomas, P. D. (2013). Large-scale gene function analysis with the PANTHER classification system. *Nature Protocols*, *8*, 1551–1566.

Minamishima, Y. A., Moslehi, J., Padera, R. F., Bronson, R. T., Liao, R., & Kaelin, W. G. (2009). A feedback loop involving the Phd3 prolyl hydroxylase tunes the mammalian hypoxic response in vivo. *Molecular and Cellular Biology*, *29*, 5729–5741.

Neitemeier, S., Dolga, A. M., Honrath, B., Karuppagounder, S. S., Alim, I., Ratan, R. R., & Culmsee, C. (2016). Inhibition of HIF-prolyl-4-hydroxylases prevents mitochondrial impairment and cell death in a model of neuronal oxytosis. *Cell Death & Disease*, *7*, e2214.

Nikić, I., Merkler, D., Sorbara, C., Brinkoetter, M., Kreutzfeldt, M., Bareyre, F. M., Brück, W., Bishop, D., Misgeld, T., & Kerschensteiner, M. (2011). A reversible form of axon damage in experimental autoimmune encephalomyelitis and multiple sclerosis. *Nature Medicine*, *17*, 495–499.

Nimlamool, W., Andrews, R. M. K., & Falk, M. M. (2015). Connexin43 phosphorylation by PKC and MAPK signals VEGF-mediated gap junction internalization. *Molecular Biology of the Cell*, *26*, 2755–2768.

Nowicka, M., Krieg, C., Crowell, H. L., Weber, L. M., Hartmann, F. J., Guglietta, S., Becher, B., Levesque, M. P., & Robinson, M. D. (2019). CyTOF workflow: Differential discovery in high-throughput high-dimensional cytometry datasets. *F1000Research*, *6*, 748.

Oosthuyse, B., Moons, L., Storkebaum, E., Beck, H., Nuyens, D., Brusselmans, K., Van Dorpe, J., Hellings, P., Gorselink, M., Heymans, S., Theilmeier, G., Dewerchin, M., Laudenbach, V., Vermylen, P., Raat, H., Acker, T., Vleminckx, V., Van Den Bosch, L., Cashman, N., … Carmeliet, P. (2001). Deletion of the hypoxia-response element in the vascular endothelial growth factor promoter causes motor neuron degeneration. *Nature Genetics*, *28*, 131–138.

Patro, R., Duggal, G., Love, M. I., Irizarry, R. A., & Kingsford, C. (2017). Salmon provides fast and bias-aware quantification of transcript expression. *Nature Methods*, *14*, 417–419.

Pelster, B., & Egg, M. (2018). Hypoxia-inducible transcription factors in fish: Expression, function and interconnection with the circadian clock. *The Journal of Experimental Biology*, *221*, jeb163709.

Pertea, M., Kim, D., Pertea, G. M., Leek, J. T., & Salzberg, S. L. (2016). Transcript-level expression analysis of RNA-seq experiments with HISAT, StringTie and Ballgown. *Nature Protocols*, *11*, 1650–1667.

Perriot, S., Mathias, A., Perriard, G., Canales, M., Jonkmans, N., Merienne, N., Meunier, C., El Kassar, L., Perrier, A. L., Laplaud, D, A., Schluep, M., Déglon, N., & Du Pasquier, R. (2018). Human induced pluripotent stem cell-derived astrocytes are differentially activated by multiple sclerosis-associated cytokines. *Stem Cell Reports*, *11*, 199–1210.

Pfaffl, M. W. (2001). A new mathematical model for relative quantification in real-time RT–PCR. *Nucleic Acids Research*, *29*, e45.

Roscoe, W. A., Welsh, M. E., Carter, D. E., & Karlik, S. J. (2009). VEGF and angiogenesis in acute and chronic MOG((35-55)) peptide induced EAE. *Journal of Neuroimmunology*, *209*, 6–15.

Rosiewicz, K. S., Crowley, T., Saher, G., Kerkering, J., Alisch, M., & Siffrin, V. (2020). Comparison of RNA isolation procedures for analysis of adult murine brain and spinal cord astrocytes. *Journal of Neuroscience Methods*, *333*, 108545.

Ruscher, K., Freyer, D., Karsch, M., Isaev, N., Megow, D., Sawitzki, B., Priller, J., Dirnagl, U., & Meisel, A. (2002). Erythropoietin is a paracrine mediator of ischemic tolerance in the brain: Evidence from an in vitro model. *Journal of Neuroscience: The Official Journal of the Society for Neuroscience*, *22*, 10291–10301.

Salman, M. M., Kitchen, P., Halsey, A., Wang, M. X., Törnroth-Horsefield, S., Conner, A. C., Badaut, J., Iliff, J. J., & Bill, R. M. (2022). Emerging roles for dynamic aquaporin-4 subcellular relocalization in CNS water homeostasis. *Brain*, *145*, 64–75.

Scemes, E., Dermietzel, R.,& Spray, D. C. (1998). Calcium waves between astrocytes from Cx43 knockout mice. *Glia*, *24*, 65–73.

Schneider, C. A., Rasband, W. S., & Eliceiri, K. W. (2012). NIH image to ImageJ: 25 years of image analysis. *Nature Methods*, *9*, 671–675.

Schwartz, M., Moalem, G., Leibowitz-Amit, R., & Cohen, I. R. (1999). Innate and adaptive immune responses can be beneficial for CNS repair. *Trends in Neurosciences*, *22*, 295–299.

Shi, Q., Liu, X., Wang, N., Zheng, X., Fu, J., & Zheng, J. (2016). Nitric oxide from brain microvascular endothelial cells may initiate the compensatory response to mild hypoxia of astrocytes in a hypoxia-inducible factor-1α dependent manner. *American Journal of Translational Research*, *8*, 4735–4749.

Siffrin, V., Radbruch, H., Glumm, R., Niesner, R., Paterka, M., Herz, J., Leuenberger, T., Lehmann, S. M., Luenstedt, S., Rinnenthal, J. L., Laube, G., Luche, H., Lehnardt, S., Fehling, H. J., Griesbeck, O., & Zipp, F. (2010). In vivo imaging of partially reversible th17 cell-induced neuronal dysfunction in the course of encephalomyelitis. *Immunity*, *33*, 424–436.

Siffrin, V., Vogt, J., Radbruch, H., Nitsch, R., & Zipp, F. (2010). Multiple sclerosis: candidate mechanisms underlying CNS atrophy. *Trends in Neurosciences*, *33*, 202–210.

Sofroniew, M. V., & Vinters, H. V. (2010). Astrocytes: Biology and pathology. *Acta Neuropathology (Berl)*, *119*, 7–35.

Sühs, K.-W., Hein, K., Sättler, M. B., Görlitz, A., Ciupka, C., Scholz, K., Käsmann-Kellner, B., Papanagiotou, P., Schäffler, N., Restemeyer, C., Bittersohl, D., Hassenstein, A., Seitz, B., Reith, W., Fassbender, K., Hilgers, R., Heesen, C., Bähr, M., & Diem, R. (2012). A randomized, double-blind, phase 2 study of erythropoietin in optic neuritis. *Annals of Neurology*, *72*, 199–210.

Sun, Q., Zhou, J., Zhang, Z., Guo, M., Liang, J., Zhou, F., Long, J., Zhang, W., Yin, F., Cai, H., Yang, H., Zhang, W., Gu, Y., Ni, L., Sai, Y., Cui, Y., Zhang, M., Hong, M., Sun, J., … Ren, Y. (2014). Discovery of fruquintinib, a potent and highly selective small molecule inhibitor of VEGFR 1, 2, 3 tyrosine kinases for cancer therapy. *Cancer Biology & Therapy*, *15*, 1635–1645.

The Gene Ontology Consortium, Carbon, S., Douglass, E., Good, B. M., Unni, D. R., Harris, N. L., Mungall, C. J., Basu, S., Chisholm, R. L., Dodson, R. J., Hartline, E., Fey, P., Thomas, P. D., Albou, L.-P., Ebert, D., Kesling, M. J., Mi, H., Muruganujan, A., Huang, X., … Elser, J. (2021). The gene ontology resource: Enriching a GOld mine. *Nucleic Acids Research*, *49*, D325–D334.

Toriuchi, K., Kakita, H., Tamura, T., Takeshita, S., Yamada, Y., & Aoyama, M. (2020). Prolonged astrocyte-derived erythropoietin expression attenuates neuronal damage under hypothermic conditions. *Journal of Neuroinflammation*, *17*, 141.

Trapp, B. D., & Stys, P. K. (2009). Virtual hypoxia and chronic necrosis of demyelinated axons in multiple sclerosis. *Lancet Neurology*, *8*, 280–291.

Urrutia, A. A., Afzal, A., Nelson, J., Davidoff, O., Gross, K. W., & Haase, V. H. (2016). Prolyl-4-hydroxylase 2 and 3 coregulate murine erythropoietin in brain pericytes. *Blood*, *128*, 2550–2560.

Van Gassen, S., Callebaut, B., Van Helden, M. J., Lambrecht, B. N., Demeester, P., Dhaene, T., & Saeys, Y. (2015). FlowSOM: Using self-organizing maps for visualization and interpretation of cytometry data. *Cytometry. Part A: The Journal of the International Society for Analytical Cytology*, *87*, 636–645.

Voskuhl, R. R., Peterson, R. S., Song, B., Ao, Y., Morales, L. B. J., Tiwari-Woodruff, S., & Sofroniew, M. V. (2009). Reactive astrocytes form scar-like perivascular barriers to leukocytes during adaptive immune

inflammation of the CNS. *The Journal of Neuroscience*, 29, 11511–11522.

Wallraff, A., Köhling, R., Heinemann, U., Theis, M., Willecke, K., & Steinhäuser, C. (2006). The impact of astrocytic gap junctional coupling on potassium buffering in the hippocampus. *J Neuro sci*, 26, 5438–5447.

Watts, D., Gaete, D., Rodriguez, D., Hoogewijs, D., Rauner, M., Sormendi, S., & Wielockx, B. (2020). Hypoxia pathway proteins are master regulators of erythropoiesis. *International Journal of Molecular Sciences*, 21, 8131.

Weber, L. M., Nowicka, M., Soneson, C., & Robinson, M. D. (2019). Diffcyt: Differential discovery in high-dimensional cytometry via high-resolution clustering. *Communications Biology*, 2, 1–11.

Wielockx, B., Grinenko, T., Mirtschink, P., & Chavakis, T. (2019). Hypoxia pathway proteins in Normal and malignant hematopoiesis. *Cell*, 8, E155.

Winchenbach, J., Düking, T., Berghoff, S. A., Stumpf, S. K., Hülsmann, S., Nave, K.-A., & Saher, G. (2016). Inducible targeting of CNS astrocytes in Aldh1l1-Cre^ERT2 BAC transgenic mice. *F1000Research*, 5, 2934.

Wood, J., Stell, R., Unsworth, I., Lance, J. W., & Skuse, N. (1985). A double-blind trial of hyperbaric oxygen in the treatment of multiple sclerosis. *The Medical Journal of Australia*, 143, 238–240.

Wood, J. M., Bold, G., Buchdunger, E., Cozens, R., Ferrari, S., Frei, J., Hofmann, F., Mestan, J., Mett, H., O'Reilly, T., Persohn, E., Rösel, J., Schnell, C., Stover, D., Theuer, A., Towbin, H., Wenger, F., Woods-Cook, K., Menrad, A., ... Totzke, F. (2000). PTK787/ZK 222584, a novel and potent inhibitor of vascular endothelial growth factor receptor tyrosine kinases, impairs vascular endothelial growth factor-induced responses and tumor growth after Oral administration. *Cancer Research*, 60, 2178–2189.

Yasuhara, T., Shingo, T., Muraoka, K., Kameda, M., Agari, T., Yuan, W. J., Hayase, H., Hamada, H., Borlongan, C. V., & Date, I. (2005). Neurorescue effects of VEGF on a rat model of Parkinson's disease. *Brain Research*, 1053, 10–18.

SUPPORTING INFORMATION

Additional supporting information can be found online in the Supporting Information section at the end of this article.